Observability of Moisture Transport Divergence in Arctic Atmospheric Rivers by Dropsondes

Henning Dorff[1,2], Heike Konow[3,1], Vera Schemann[4], and Felix Ament[1,3]

[1]University of Hamburg, Hamburg, Germany

[2]International Max Planck Research School on Earth System Modelling, Max Planck Institute for Meteorology, Hamburg, Germany

[3]Max Planck Institute for Meteorology, Hamburg, Germany

[4]University of Cologne, Cologne, Germany

Correspondence: henning.dorff@uni-hamburg.de

Abstract. This study emulates dropsondes to elucidate ~~how adequately~~ the extent to which sporadic airborne sondes adequately represent divergence of moisture transport in arctic Atmospheric Rivers (ARs). The convergence of vertically integrated moisture transport (IVT) plays a crucial role as it favours precipitation that significantly affects arctic sea ice properties. ~~Long range~~ Long-range research aircraft can transect ARs and drop sondes to determine their IVT divergence. In order to assess the representativeness of future sonde-based IVT divergence in arctic ARs, we disentangle ~~errors~~ deviations arising from undersampling by discrete soundings and from the flight duration.

Our synthetic study uses CARRA reanalyses to set up an idealised scenario for airborne AR observations. For nine arctic spring ARs, we mimic flights transecting each AR in CARRA and emulate sonde-based IVT representation by picking single vertical profiles. The emulation quantifies IVT divergence observability by two approaches. First, sonde-based IVT and its divergence are compared to the continuous IVT interpolated onto the flight cross-section. The comparison specifies uncertainties of discrete sonde-based IVT variability and divergence. Second, we determine how temporal AR evolution affects IVT divergence values by contrasting time-propagating sonde-based values with the divergence based on instantaneous snapshots.

For our arctic AR cross-sections, we find that coherent wind and moisture variability contribute by less than 10 % to the total transport. Both quantities are uncorrelated to a great extent. Moisture turns out as the more variable quantity. We show that sounding spacing greater than 100 km results in errors greater than 10 % of the total IVT along AR cross-sections. For IVT divergence, the arctic ARs exhibit similar differences in moisture advection and mass convergence across the embedded front as mid-latitude ARs, but we identify moisture advection being dominant. Overall, we confirm their observability with an uncertainty of ~~up to 25~~around 25–50 % using a sequence of at least seven sondes per cross-section. Rather than sonde undersampling, it is the temporal AR evolution over the flight duration that leads to ~~higher~~ high deviations in divergence components. Dedicated planning of sonde-based IVT divergence purposes should not only involve sonde positioning~~but rather~~ , but also pursue optimizing the flight duration. Our benchmarks ~~quantify~~ identify sonde-based uncertainties as a prerequisite to be used for future airborne moisture budget closure in arctic ARs.

1 Introduction

~~ARs~~Atmospheric Rivers (ARs), which are elongated (> 2000 km in length) but narrow (< 1000 km in width) water vapour rich corridors with ~~high~~ strong moisture transport, occasionally enter the Arctic. Their occurrence accounts for roughly 70 % of poleward moisture transport (Nash et al., 2018). The presence of ARs can induce significant ~~Arctic~~ arctic warming (e.g. Neff et al., 2014) causing substantial sea-ice retreat (Woods and Caballero, 2016) as well as Greenland ice sheet melt (Mattingly et al., 2018; Neff, 2018). In addition to near-surface heat fluxes (Woods and Caballero, 2016; You et al., 2022), the melting arises from AR-induced precipitation (Mattingly et al., 2018; Viceto et al., 2022). Lauer et al. (2023b) identified ARs as one of the main contributors to overall arctic precipitation. ~~The moisture needed for this is mainly extracted more southern, with~~ For the required moisture of ARs impacting the Arctic, the North Atlantic ~~being a dominant moisture~~ to the south is a dominant uptake zone (Vázquez et al., 2018). ~~In an interplay with~~ Embedded in poleward moving cyclones and their warm conveyor belts (e.g. Dacre et al., 2019), the AR air masses can propagate ~~meridionally~~ meridional towards the Arctic ~~ocean~~ Ocean and reach the sea-ice (Papritz et al., 2021), shaping the regional moisture patterns (Nygård et al., 2020). Along the long-distance displacement, the AR embedded moist and warm air masses are subject to ~~substantial air mass transformation~~ transforming thermodynamic vertical structures (You et al., 2022). Komatsu et al. (2018) discovered an amplification of ~~air mass transformation~~ the air mass transformations after the ARs overpass the sea-ice edge.

To illuminate moisture transformation processes occurring in arctic ARs, it is crucial to grasp spatial characteristics of the moisture transport, i.e. the vertically Integrated Water Vapour Transport (IVT). For instance, Seager and Henderson (2013) point out that the divergence of IVT links the local temporal ~~evolution~~ development of moisture amount ~~to~~ with the efficiency of precipitation ~~induction. In order~~ formation. When we thus target to derive IVT divergence ~~,~~ in ARs, a prerequisite is to resolve the spatial variability of IVT~~in ARs needs to be resolved. Guan and Waliser (2015) considered~~ . Guan and Waliser (2015) used global ECMWF Interim reanalysis (ERA-Interim, Dee et al., 2011) to ~~specify~~ investigate strong moisture transport gradients that exist along AR cross-sections, perpendicular to the major IVT orientation. Along such lateral cross-sections through the AR ~~center,~~ centre, airborne observations in mid-latitude ARs have shown a bell-shaped IVT distribution, having the strongest moisture transport in the AR core ~~, is widely seen from airborne observations in mid-latitude ARs~~ (e.g. Ralph et al., 2017; Demirdjian et al., 2020). Using ERA5, Cobb et al. (2021b) confirm ~~this heterogeneous~~ the high spatial variability of IVT for mid-latitude ARs. For ~~arctic AR conditions with~~ the conditions in arctic ARs containing weaker moisture transport than in the mid-latitudes, we still lack quantitative knowledge of predominant IVT variability and how this ~~reflects to~~ influences IVT divergence.

High-resolution observations of IVT variability ~~to derive its divergence in ARs are missing for the Arctic~~are not available for arctic ARs. One reason is the remote and ~~sporadic~~ infrequent occurrence of arctic ARs over the ocean basins. Furthermore, the observation of moisture transport requires simultaneous measurements of winds and moisture for the entire troposphere. Radiosondes allow detailed insights of moisture transport profiles of arctic ARs at individual locations (e.g. Viceto et al., 2022), but their observation network in the Arctic is too sparse to obtain the divergence in single ARs (Dufour et al., 2016). ~~Similarly~~Based on a similar principle, dropsondes released from research aircraft ~~can~~ provide vertical profiles of relative humidity and wind speed with an accuracy of 1 % and 0.1 m/s, respectively (e.g. George et al., 2021; Konow et al., 2021). The simultaneous measurements allow ~~to derive~~ derivation of moisture transport profiles and IVT. According to Zheng et al. (2021), dropsondes over ocean fill a data gap left by spaceborne remote sensing or ground-based observations. To derive the IVT divergence in ARs, it is necessary to release the sondes at close spacing but over horizontally extended areas above the AR, which can only be achieved by long-range research aircraft (Neiman et al., 2014).

The overall goal of this study is to assess the observability of moisture transport divergence in arctic ARs by dropsondes~~in order to facilitate dedicated research flight campaigns and measurement strategies~~. The assessment targets the facilitation of measurement strategies in dedicated research flights, as e.g. proposed by Wendisch et al. (2021). ~~This assessment comprises~~ It includes (a) the role of ~~sounding frequency, the influence of correlated~~ sonde frequency, (b) concretising the need for supplementary measurements based on individual moisture and wind ~~fields on moisture transport,~~ variability, and c) the impact of extended flight duration under evolving AR conditions on the ability of the dropsondes to reproduce IVT divergence in arctic ~~ARs and the impact of extended flight duration.~~ ARs. The following paragraphs set these aspects into context ~~with~~ of recent findings based on mid-latitude ARs and unravel four research gaps for arctic ARs, summarised as guiding ~~science~~ questions.

~~Deteriorations~~ A limited number of sondes can cause deviations in the airborne representation of AR moisture transport variability ~~can result from a limited number of sondes~~ if the sounding spacing becomes too coarse to reflect the spatial variability of IVT. ~~The sondes may misinterpret~~ Such deviations in IVT variability come with misinterpretation of the IVT divergence. For mid-latitude ARs, Guan et al. (2018) compared sonde-based Total Integrated Water Vapour Transport ($TIVT$), ~~being~~ the integral of IVT along an AR cross-section, with reanalysis-based $TIVT$ and found an agreement up to 3 % ~~for airborne results~~ based on a mean sounding spacing of 80 km. ~~Contrasting the airborne~~ Accurate airborne estimates of $TIVT$~~in~~, juxtaposed for two separate AR cross-section legs~~can serve as~~, provide an initial estimate of IVT divergence in between both legs. However, Ralph et al. (2017) found considerable sensitivity of sonde-based $TIVT$ to the spacing between the sonde spacing. Enlarging the ~~initial spacing between the sondes~~ aforementioned sonde spacing by reducing the number of included sondes, they found a mean deviation of at least 5 % for $TIVT$ when doubling the spacing. Since given sensitivity studies refer purely to mid-latitude cases where we do expect higher $TIVT$ (Guan et al., 2018), it remains as open question: *What is the maximum distance between sondes to determine the total moisture transport in arctic AR cross-sections (Q1)?*

When assessing spatial IVT variability in arctic ARs, it ~~becomes~~ is crucial how moisture and wind fields coincide in the AR cross-section or whether they contribute independently to ~~the~~ IVT variability. For instance, in a polar AR case study, Terpstra et al. (2021) identified incoherent patterns of moisture and wind ~~that form~~ forming the moisture transport ~~patterns but~~ pattern, that are less aligned than in mid-latitude ARs. ~~The disentanglement of both quantities facilitates flight strategies in the observation of~~ Unravelling moisture transport into wind and moisture can improve observational strategies of airborne moisture transport divergence in arctic ARs. ~~If~~ Especially, if the moisture transport variability (and divergence) were e.g. mainly controlled by the moisture field, ~~more investment should be spent on~~ supplementary remote-sensing should be involved in the airborne representation of AR moisture~~by supplementary measurements.~~. For this reason, it is important to determine whether moisture and wind are aligned in AR cross-sections and to ascertain: *How correlated are moisture and winds in arctic ARs and do coherent patterns contribute significantly to IVT (Q2)?*

Knowing the spatial structure of IVT is ~~an essential~~ a prerequisite for flight planning and reveals insights into the moisture transport divergence pattern in arctic AR cross-sections. Since ARs primarily occur ~~in conjunction with a cold front~~ at the interface of the cold front and warm conveyor belt in extratropical cyclones Dacre et al. (2019), different dynamic and thermodynamic processes act on the moisture transport and its divergence across the embedded front (Cobb et al., 2021a). For mid-latitude ARs, Cobb et al. (2021a) found significant differences ~~of~~ in vertical moisture and wind ~~domains~~ for different sectors before and behind the front, which are reflected in gradients in the IVT divergence across the front ~~which transfer to frontal gradients in divergence characteristics~~ (Guan et al., 2020). Using reanalysis data, Guan et al. (2020) specified lateral differences of moisture transport divergence across ~~centers~~ centres of ARs. In the AR ~~center~~ centre with maximum IVT, they identified the dynamical convergence of moisture as the most prominent component regulating moisture amount and precipitation. The Arctic is more affected by exit regions of ARs rather than over-passed by AR centres and exhibits weaker IVT from ARs compared to the mid-latitudes (Guan and Waliser, 2019). ARs here commonly start dissipating and terminating (Guan et al., 2023). For such conditions, we lack knowledge of predominant IVT divergence. Thus, we examine: *How can the divergence of moisture transport be characterised along cross-sections of arctic ARs (Q3)?*

Norris et al. (2020) ~~conducted airborne studies to determine~~ determined IVT divergence in mid-latitude ARs from dropsondes. ~~Such research flights allow to interpret the discrepancies~~ Their research flight allows interpreting quantitive discrepancies of IVT divergence in ARs that Guan et al. (2020) found between ~~reanalyses in representing IVT divergence in ARs. In contrast,~~ different reanalyses. Norris et al. (2020) point to the large variability of IVT divergence at spatial scales of 50~~km~~ km, which has implications for sonde-based ~~results~~sampling best practices. For arctic AR conditions, we lack equivalent estimates. Moreover, besides sonde-based under-sampling of IVT variability and divergence, we hypothesise that airborne results are ~~also impaired by a time component. Over~~ impaired by the flight duration: Over the duration required to enclose an AR corridor, the atmospheric state changes, i.e. there is relevant temporal evolution of the AR (its life cycle and spatial displacement) ~~can affect~~ that causes the sonde-based ~~results significantly. Before~~ values to deviate from the instantaneous IVT divergence. Hence, before dropsondes are used to interpret the actual IVT divergence in arctic ARs, we have to disentangle sonde-based errors that arise from undersampling by discrete sounding and from non-instantaneous sampling over the flight duration. We quantify: *To what extent do non-instantaneous sondes reproduce IVT divergence in the light of the AR evolution during flight (Q4)?*

To pursue Q1-Q4, we focus on ARs occurring over the Arctic ~~ocean~~ Ocean (i.e. Fram Strait and Greenland Sea) in the vicinity of the sea-ice edge due to the above-mentioned AR impacts on the sea-ice. We ~~constrain on~~ restrict our analysis to ARs during spring, when maximum sea-ice extent starts melting. We look at arctic ARs within the novel C3S Arctic Regional Reanalysis (CARRA). Introducing a flight strategy to analyse moisture transport divergence in arctic AR corridors, we consider arctic AR events along synthetic flight tracks that transect an AR corridor. We emulate synthetic dropsondes along the tracks by depicting single vertical profiles. This study compares actual IVT variability and divergence along the flight tracks with the emulated sonde-based representation of IVT in order to assess how adequately such airborne perspectives reproduce predominant AR-IVT characteristics. In a nutshell, our synthetic assessment provides benchmarks of sonde-based uncertainties in their representation of IVT divergence in arctic ARs to facilitate future mission planning.

The ~~remainder of the~~ manuscript is structured as follows: After introducing our AR cases, Section 2 describes the methods

Table 1. Specifications of used reanalyses for AR analysis

Reanalysis Dataset	Horizontal Resolution	Vertical resolution up to 10 km (≈ 250 hPa)	Time resolution
ERA5	0.25 x 0.25 deg	21 levels	hourly
CARRA	2.5 x 2.5 km	15 levels	hourly

of emulating dedicated flight patterns and synthetic soundings, and how we derive moisture transport divergence. For this framework, Section 3 deals with the IVT variability. This entails the total moisture transport and ~~the~~ IVT variability along cross-sections in arctic ARs, their sonde-based representation (Q1) and the coherence of moisture and winds (Q2). Section 4 specifies the moisture transport divergence in arctic ARs (Q3) and compares its continuous representation to that by sporadic sondes. Section 5 quantifies airborne deviations arising from AR evolution over flight duration that is mostly idealised as stationary (Q4).

2 Airborne derivation of moisture transport divergence in arctic ARs

The central quantity of our study is the Integrated Water Vapour Transport (IVT) that represents the AR intensity as:

$$IVT = -\frac{1}{g} \cdot \int_{p_{\mathrm{sfc}}}^{p_{\mathrm{top}}} q\mathbf{V}\,dp \qquad (1)$$

where $\mathbf{V}$ is the horizontal wind vector and q the specific humidity. The divergence of IVT represents a key component contributing to the overall atmospheric moisture budget. Following Seager and Henderson (2013), the vertically integrated moisture budget components consist of:

$$\underbrace{\frac{\delta IWV}{\delta t}}_{\text{local change in Integrated Water Vapour}} = \underbrace{E}_{\text{Evaporation}} - \underbrace{P}_{\text{Precipitation}} - \underbrace{\nabla IVT}_{\text{Divergence of Integrated Water Vapour Transport}}, \qquad (2)$$

with all components in kilogram per metre squared per second. Precipitation and evaporation refer to surface values, while the integrated water vapour IWV and IVT (Eq. 1) represent the vertically integrated quantities of moisture and moisture transport. Note that Eq. 2 neglects the moisture flux through a tilted bottom pressure surface that is included in Seager and Henderson (2013).

Given the relevance of IVT to the AR moisture budget, this feasibility study targets the overall observability of IVT and its divergence (∇IVT) in arctic ARs by airborne sondes in a synthetic way. For this purpose, this section introduces the reanalysis framework we use to investigate a presented selection of arctic ARs. In addition, our airborne flight strategy to derive ∇IVT in arctic ARs is specified and how we emulate the synthetic sondes in the reanalyses. Lastly, we describe the sonde-based derivation of ∇IVT and how we categorise different sectors across the AR front to examine the divergence.

2.1 Reanalysis framework

This study investigates arctic ARs in a reanalysis framework (Tab. 1). We use ECMWF Reanalysis v5 (ERA5) (Hersbach et al., 2020) to identify the AR events of our interest. ERA5 outperforms other global reanalyses with respect to AR characteristics (Graham et al., 2019; Cobb et al., 2021b). Thus, recent studies consider ERA5 to investigate AR conditions specifically in the Arctic (e.g. Fearon et al., 2021; Zhang et al., 2022). At the Fram Strait and Greenland Sea, the lat-lon grid from ERA5 yields approximately 30 km distances. Given the flight performance of long-range research aircraft (see Stevens et al., 2019), the spacing of airborne soundings in such a resolution would require releases every 2 minutes, which are more frequent than conducted in recent campaigns (e.g. Ralph et al., 2017). Still, Skamarock et al. (2014) emphasise that the effective ~~resolution of processes in simulations~~ model resolution is much greater than the model grid spacing. ~~However, if~~ Since our study aims to assess the sub-grid scale variability of moisture transport between sonde releases from reanalyses, the effective resolution should be of the order of ~ 10 km rather than of ~ 100 km.

Therefore, we further include the C3S Arctic Regional Reanalysis (CARRA). CARRA has a 2.5 km horizontal resolution over the entire domain and is accessible by Schyberg et al. (2021). Driven by lateral boundary conditions from ERA5, CARRA includes more observations and hourly forecasts by the HARMONIE-AROME model (Bengtsson et al., 2017). Køltzow et al. (2022) verified the improved representation of arctic surface-near meteorological conditions in CARRA, with decorrelation lengths of wind speed in better agreement to reference observations than ERA5.

Both reanalyses are provided on pressure levels by the Copernicus Climate Data Store (CDS). While ERA5 contains IVT as output, we calculate IVT in CARRA by the trapezoidal integral of moisture transport along the pressure levels (Tab. 1). In the following, we declare the high spatial resolution representation in CARRA as our ~~idealised background~~ synthetic reality of AR features.

2.2 Selection of Atmospheric River cases

The transformation of arctic air masses over changing surface types (open ocean and sea-ice) along large-scale meridional circulations is part of current research and investigated by research aircraft over the Arctic ~~ocean~~ Ocean (Wendisch et al., 2021). For this reason, our study selects ARs causing air masses to overshoot the sea ice edge in this region. The ~~principle~~ principal identification of arctic AR events is based on the IVT-based AR detection catalogue by Guan (2022) applied to ERA5 (Lauer et al., 2023a). Among these ARs, we focus on ~~the springseason~~spring, when maximum sea-ice extent in the Arctic ~~ocean~~ Ocean starts to break-up and ~~reacts very prone~~ is more vulnerable to the intrusion of warm and moist air (Rostosky and Spreen, 2023). We restrict to ~~conditions and events only from~~ selected events from the last decade, as the arctic climate has witnessed rapid and intense changes over the last decades (Wendisch et al., 2023). Our AR pathways originate from the North Atlantic and Barents Sea, that Papritz et al. (2021) spot as dominant regions for arctic moisture intrusions. The selection constrains on ARs whose lateral width is purely situated over open ocean or sea-ice. This ensures that we do not encounter orographic induced effects on ∇IVT which are out of the scope of this study. Moreover, airborne sonde releases over land are more complicated to ~~be conducted~~conduct. Given the criteria above, we selected ARs from nine spring days between 2011 and 2020 ~~, presented~~

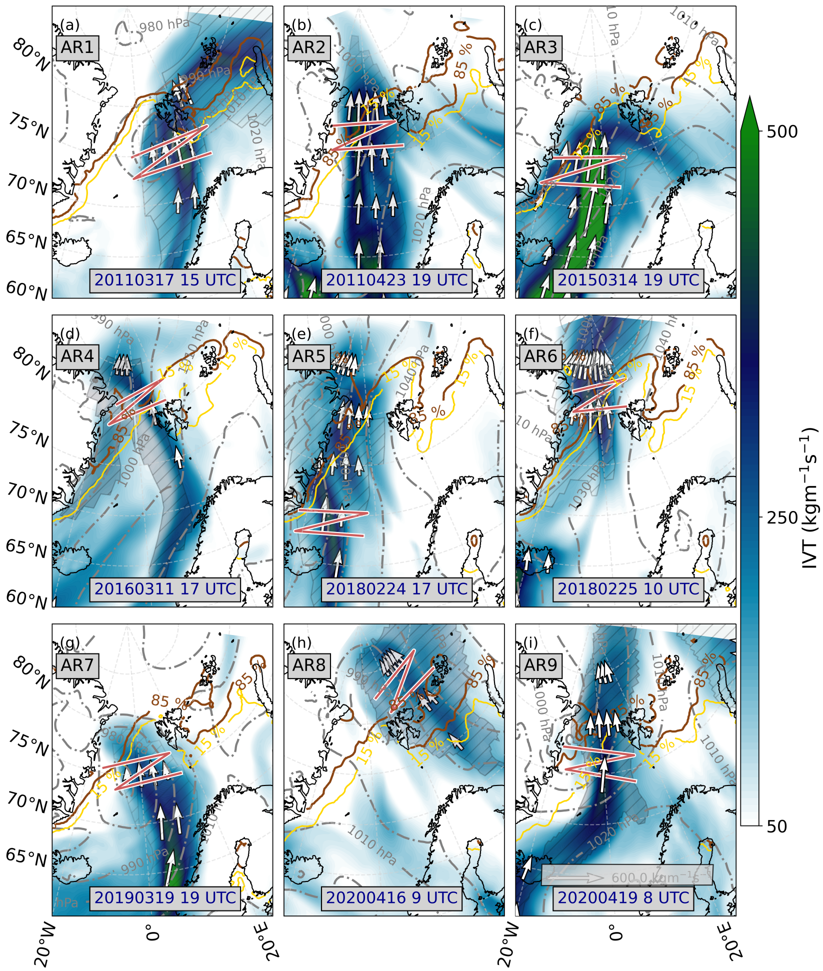

Figure 1. IVT contours of investigated AR events from ERA5. Grey lines indicate surface isobars, while brown (orange) contour lines specify sea ice cover thresholds, given in %. The arrows depict the magnitude and orientation of IVT. Hatches represent the AR boundaries defined in Guan (2022). Red lines represent the ~~zig-zag~~ zigzag flight ~~patterns~~ pattern to investigate the moisture budget in AR corridors. Background maps were made with Natural Earth.

~~in~~ (Fig. 1).

~~In the synoptic composition of a Greenland trough,~~ Greenland troughs are synoptic situations where low-pressure systems force large-scale meridional transport~~where ARs can commonly evolve~~ , with ARs potentially evolving on the eastern ~~cyclone flank and reach~~ flank of the cyclone and reaching into the Arctic (Papritz and Dunn-Sigouin, 2020). Similarly, blocking situations over Eurasia can ~~favor~~ favour meridional circulation. For our nine ARs (Fig. 1), we confirm a large case-to-case ~~variability regarding the synoptic situation~~synoptic variability. While some ARs (AR2, AR3, AR4, AR9) have evolved along the eastern flank of large-scale troughs over Greenland, AR5 and AR6 are more steered by blocking high pressure over the Barents Sea.

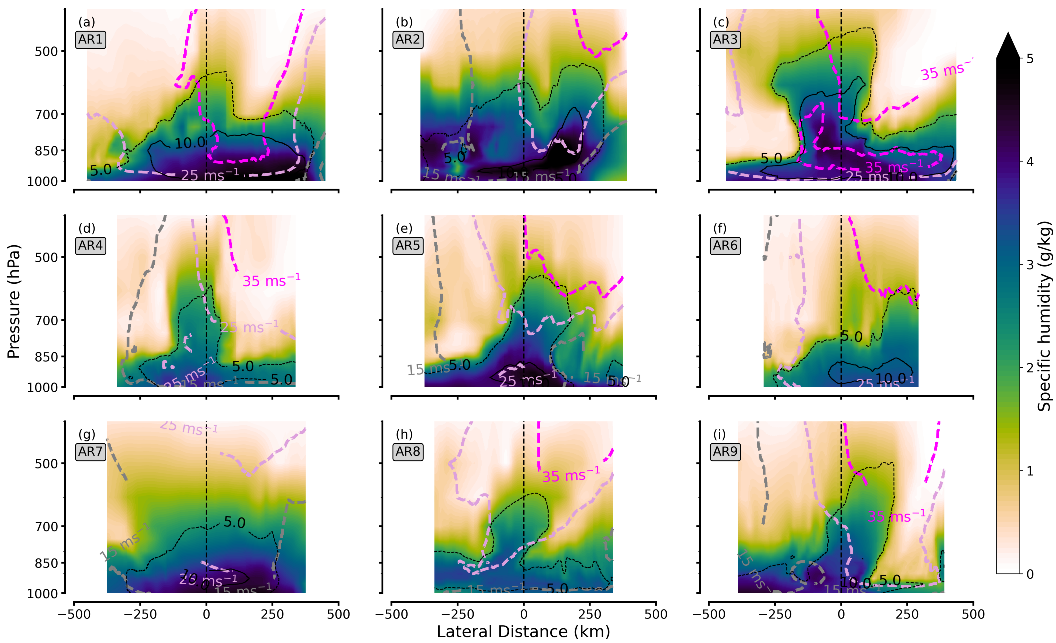

Figure 2. CARRA-based cross-sections of AR inflow legs for moisture (colour-coded contours), as well as contour lines of wind speed (pinkish) and moisture transport (black contour lines). Shown moisture transport values have the unit $\mathrm{g\,kg^{-1}\,m\,s^{-1}}$. As visible in Fig. 1, some ends of the cross-sections already reach out of the ARs, but this constitutes less than 10 % of the cross-section lengths.

AR1 and AR7 are, in turn, reinforced by a mesoscale cyclone situated over the Fram Strait and reach very close into the cyclone ~~center~~centre.

The synoptic compositions lead to AR ~~dispersions~~ dispersion over the North Atlantic and Arctic Ocean (Fig. 1), which correspond to the typical arctic moisture transport pathways identified in Papritz et al. (2021). Some ARs exhibit straight meridional moisture transport north of Iceland and approach or exceed Svalbard (AR1, AR2, AR3 in Fig. 1). AR4 and AR7 show more elongated filaments along the Norwegian coast, but still reach far north. We consider eight independent AR events, wherein AR5 is also considered for the consecutive day (AR6). At this stage, the centre of AR6 reaches close to the North Pole. AR8 originates from Siberia that, according to Komatsu et al. (2018), represents another significant roadway for arctic moisture intrusions ~~favoring~~ favouring ARs. The last events in 2020 (AR8, AR9) are accompanied by a warm air intrusion period observed by the Multidisciplinary drifting Observatory for the Study of Arctic Climate (MOSAiC) expedition (Shupe et al., 2022), studied in Kirbus et al. (2023).

~~glt!~~ Inspecting the vertical curtains of AR cross-sections, that are based on the southern red transects in Fig. 1, the specific humidity exceeds $4\,\mathrm{g\,kg^{-1}}$ in almost every cross-section (Fig. 2). This indicates that our events are rather moist for arctic AR conditions (e.g. Viceto et al., 2022), but still much drier than mid-latitude ARs where q easily exceeds $8\,\mathrm{g\,kg^{-1}}$ (Cobb et al., 2021a). Nonetheless, Fig. 2 depicts several features that we normally know from mid-latitude ARs. For example, this comprises low-level jets (LLJs) that are strong low-level wind corridors (Ralph et al., 2004; Demirdjian et al., 2020). For the windy arctic

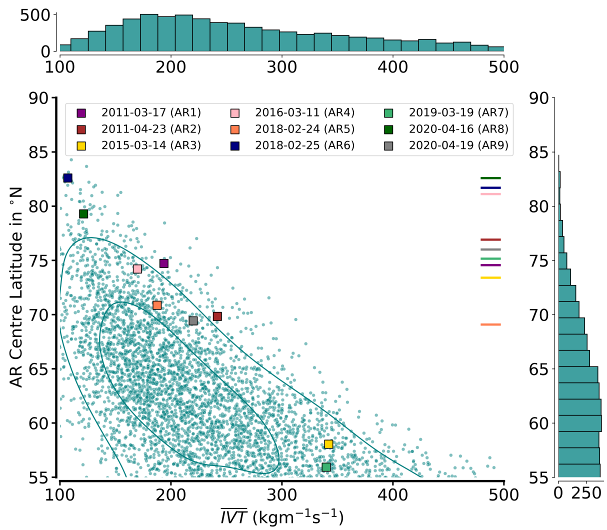

Figure 3. Comparison of selected AR events to long-term statistics (1979–2019) regarding mean ~~IVT~~ *IVT* and AR centre latitude at given reanalysis time step (ERA-Interim) based on the AR catalogue of Guan (2022). Isolines represent 25th and 75th percentiles of the kernel density estimate. Coloured lines on the right indicate the centre of the respective flight pattern.

AR events, e.g. AR3 and AR5, we detect the presence of LLJs stronger than 25 m s^{-1}. The LLJ is situated at a height of around 900 hPa, slightly lower than Cobb et al. (2021a) summarised for mid-latitude ARs. Ralph et al. (2004) and Cordeira et al. (2013) found a horizontally slanted vertical structure of moisture transport in mid-latitude AR cross-sections from dropsondes and reanalyses. Ralph et al. (2017) verified the vertical interaction between the upper-level jet and the LLJ as dominant for AR moisture transport. In Fig. 2, their conceptual depictions reflect mostly for AR5. Here, moist air masses residing in the cyclonic warm conveyor belt are lifted over the cold front sector. The downward intrusion of the upper-level jet on the western flank causes the slanted structure in the moisture transport.

In other arctic ARs than AR5, we find less agreement with the conceptual AR schemes presented in Ralph et al. (2017). This yields for the vertical structure of moisture, the presence and the intensity of the LLJ which is strongly distinctive in AR1, AR3, AR5, AR7, but missing there. In some cases, e.g. AR9, the upper-level jet intrusion is accompanied by strong dry air subsidence that reinforces the slanting of the moisture transport pattern in the mid and lower levels. The variety of characteristics of winds, moisture, and its transport comes with the different synoptic patterns (such as troughs, ridges, smaller cyclones embedded in a meridional, but weaker flow) that cause the arctic ARs. For example, we find the slanting most effective for ARs close to Eastern Greenland (AR2) or when the backside of the embedded cyclone strongly advects the dry Greenland air masses (AR9).

A caveat of our AR selection for making general statements about ~~*IVT*~~ moisture transport variability in arctic ARs is the small sample size (nine ~~AR~~ events). Therefore, we place our events in the climatology for arctic ARs in spring. Using the entirety of spring ARs along the Atlantic pathway from the catalogue of Guan (2022), we compare the latitude of the AR centres and mean IVT of our ARs with the long-term distribution (1979–2019) for spring ARs (Fig. 3). The climatological distribution in Fig. 3 indicates the decrease of mean IVT with meridional location of the AR centre. Further towards the Arctic, ARs become weaker and when centered centred north of 65°N, the mean IVT remains below $300\,\mathrm{kg\,m^{-1}\,s^{-1}}$. This is also the case for our AR eventsbut they, in turn, are characterized by a higher intensity relative . However, for their specific latitude, the ARs are often characterized by higher IVT compared to the long-term mean (Fig. 3). Only AR3 and AR7 are centred below 60°N, aligned with mean IVT values around $350\,\mathrm{kg\,m^{-1}s^{-1}}$. HoweverStill, despite their southern centre, they reach far north with $IVT > 250\,\mathrm{kg\,m^{-1}s^{-1}}$ inside the Fram Strait (Fig. 1), so that we declare them as arctic ARs. We conclude from Fig. 3 that our cases represent the stronger AR events occurring in the Arctic.

2.3 Flight pattern and emulated observationsEmulating flight patterns to sample ARs

Having introduced our AR cases, this subsection returns Returning to the perspective of the airborne observability of ∇IVT inside arctic ARs. We describe the emulation of real observations by mimicking dedicated flight patterns and creating synthetic soundings.

2.3.1 Zig-zag flight tracks observing AR corridors

For the airborne derivation of moisture transport divergence, flight patterns have , we need a dedicated flight pattern. Such a pattern has to well sample specific corridors of the AR. In general, flight Flight tracks enclosing corridors, e.g. circles, allow divergence calculations best and are frequently applied for such purposes (e.g. Bony and Stevens, 2019). However, ARs exhibit cross-frontal heterogeneity in moisture and wind fields (Cobb et al., 2021a) that would smooth out in single circles. Instead, the high lateral variability in AR moisture transport characteristics requires long flight legs across the AR front filament to better capture divergence heterogeneity. Two parallel cross-sections can be connected via an internal flight leg, resulting in a zig-zag zigzag flight pattern (Fig. 4a). The zig-zag zigzag pattern observes corridors of the AR across its transport direction. The boundary cross-section legs perpendicular to the major flow quantify focus on quantifying the corridor in- and outflow, i.e. in- and outgoing IVT over the entire lateral AR extension and enable simplified divergence calculations. Note that the diagonal internal legs can assess focus on assessing precipitation rate, evaporation, or water load inside the AR corridor so that this pattern additionally allows to quantify allows quantifying the remaining moisture budget components . According to Fig. 1, we place such zig-zag of the budget box, i.e. AR corridor (Fig. 4b).

We place the zigzag flight patterns over AR corridors at the sea ice edge . The (Fig. 1). We orientate the cross-section legs orientate orthogonal to the major IVT direction and extend the legs such that they cross transect the entire AR, as long as the legs AR boundaries remain over open ocean and sea ice and disregard land. As depicted in Fig. 3, the flights transecting the AR corridors close to the sea-ice are mainly located We obtain the boundaries from the AR catalogue of Guan (2022). The meridional distance between both cross-sections is assured to be larger than 200 km, but closer than half the lateral AR width. The final distance is chosen individually by visual inspection, as we allow flexibility for the actual flight planning. Due to their proximity to the sea ice edge, the transects of AR corridors are mainly north of AR centres (horizontal lines in Fig. 3).

For the airborne representation, we mimic We mimic the airborne AR representation by the flight performance of state-of-

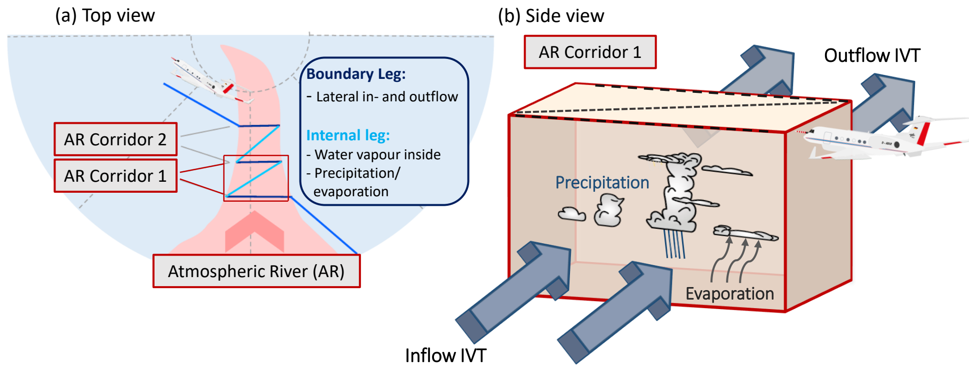

Figure 4. Top (a) and side (b) view on envisioned ~~zig-zag~~ zigzag flight pattern to derive the moisture budget components inside AR corridors.

the-art long-range research aircraft. We refer to the High Altitude and LOng Range Research Aircraft (HALO), equipped with dropsondes and a remote sensing configuration (Stevens et al., 2019; Konow et al., 2021); a similar aircraft like the one examining pacific ARs, specified in Cobb et al. (2022). Both aircraft allow along-track observations during flight at common cruising levels above 10 km and a ground speed of around 250 m/s. Accordingly, we idealize flights with a constant ground speed of 250 m s^{-1} but neglect the duration for turns and choose a constant flight altitude of 10 km. From this, we represent the aircraft location in a 1 Hz resolution, in line with the operational resolution of common airborne remote-sensing products (e.g. Mech et al., 2014; Konow et al., 2019) that ~~can~~ support dropsonde data. The ~~zig-zag patterns , shown in~~ zigzag patterns (Fig. 1~~,~~) require roughly 2–3 h to be flown, and up to 1 h for single AR cross-sections.
Using this idealised flight performance, up to three reanalysis time steps represent atmospheric conditions during the flights. We upsample the reanalysis data to minutely frequency by linear time interpolation. For our 1 Hz representation of flight location, we depict the reanalysis values from the nearest minute and spatially interpolate them along the flight using ~~harvesine~~ haversine distances. This evolving representation of meteorological values and AR characteristics will from now on be referred to as "continuous AR representation". Admittedly, the upsampling ~~leaves the model physics~~ cannot assure model physics as at intermediate time steps. However, we declare the interpolation as a suitable estimate of airborne atmospheric observations in dynamic systems like ARs that are subject to significant spatial displacement.

2.3.1 ~~Synthetic dropsondes~~

2.4 Divergence derived from synthetic sondes

We synthetically refer to the measurement principle of dropsondes (Sect. 1). Along the continuous airborne AR representation of the cross-sections (Sect. ~~??~~2.3), we depict profiles as synthetic soundings for which we neglect any vertical drift or fall time. We also neglect any measurement uncertainties. Such effects are out of the scope of this study, and assumed to cause lower deviations than our considered effects. Our sondes observe exact IVT values at ~~their~~ the release position. ~~Accordingly~~Instead, we focus on the spatial representativeness of sporadic sonde-based IVT and evaluate the uncertainties in the lateral variability of moisture transport, and how these uncertainties affect the airborne non-instantaneous perspective on IVT divergence in arctic ARs.

2.5 ~~Sonde-based divergence derivation~~

To derive ∇IVT in AR corridors from sondes, a simplified approximation relies on deriving the Total Integrated Water Vapour Transport ($TIVT$) of both cross-section legs in Fig. 4. ~~Following Ralph et al. (2017) ,~~ Ralph et al. (2017) defines $TIVT$ of a cross-section ~~is defined~~ as:

$$TIVT = \int IVT\,dx, \tag{3}$$

representing the lateral integral of IVT over the flight distance x in a respective cross-section flight leg. Neglecting the moisture flux ~~that exists~~ apart from perpendicular to the flight track, i.e. missing fluxes across the eastern and western boundaries, we can approximate ∇IVT in an AR corridor by the difference of out- minus ingoing $TIVT$ of the cross-sections. ~~However, this excludes any divergence of the flow perpendicular to the cross-section.The Gaussian Theorem sets the moisture flux over the perimeter of a closed surface equal to its divergence. However, our flight pattern (Fig. 4) has open boundaries at the outer sides. Only if~~ Only if the lateral flow can confidently be neglected, we can obtain the divergence ~~by subtracting the inflow in the entrance leg from the streamward outflow~~appropriately. Given this limitation, Lenschow et al. (2007) alternatively suggests the regression method. Under linear variations, a meteorological quantity Φ (e.g. wind speed) that is stationary in time can be inferred as:

$$\Phi = \Phi_o + \frac{\delta\Phi}{\delta x}\cdot\Delta x + \frac{\delta\Phi}{\delta y}\cdot\Delta y, \tag{4}$$

with the area mean value Φ_o and Δx and Δy being zonal, meridional displacements from the area centre point. Using the values of Φ at sounding locations and minimising the least-squared errors in the linear regression fit of Eq. 4, we obtain a linear estimate of zonal (x) and meridional (y) gradients, along with the mean mesoscale value for Φ. Adding up both gradients, we calculate the divergence. Bony and Stevens (2019) and George et al. (2021) proved the feasibility of this method by comparing its divergence values with the Gaussian-based line integral over flown circles.

Having the mathematical expression, we view on the impact of IVT divergence. The divergence of moisture transport can be split up into two components:

$$\nabla IVT = -\frac{1}{g\cdot\rho_w}\cdot\int_{p_{\mathrm{sfc}}}^{p_{\mathrm{top}}}\nabla\left(q\mathbf{V}\right)dp = \underbrace{\frac{1}{g\cdot\rho_w}\cdot\int_{p_{\mathrm{sfc}}}^{p_{\mathrm{top}}} q\left(-\nabla\mathbf{V}\right)dp}_{\text{dynamical mass convergence (CONV)}} + \underbrace{\frac{1}{g\cdot\rho_w}\cdot\int_{p_{\mathrm{sfc}}}^{p_{\mathrm{top}}}\mathbf{V}\left(-\nabla q\right)dp}_{\text{integral of horizontal moisture advection (ADV)}} \quad . \tag{5}$$

The first term represents the dynamical mass convergence, being the product of the moisture mass and divergence. The mass convergence term can be related to vertical velocity via the continuity equation and itself is closely linked to precipitation (Wong et al., 2016; Norris et al., 2020). The second term represents the horizontal advection of moisture that Guan et al. (2020)

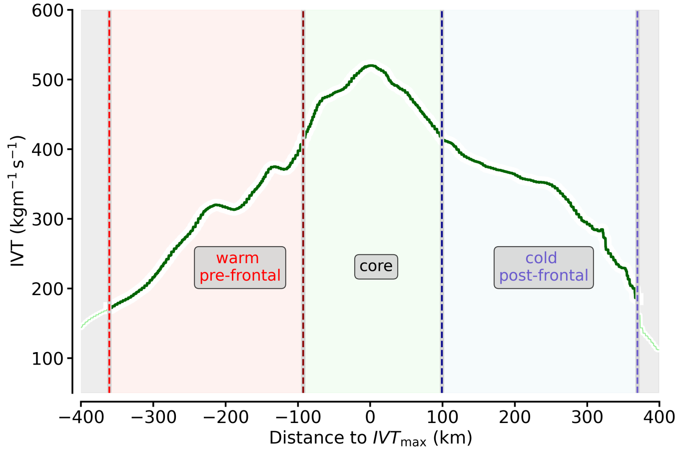

Figure 5. ~~Frontal sector~~ Sector decomposition for an ~~exemplary~~ example IVT cross-section (AR1) using the criteria described in Sect. ~~??~~2.5. The ~~colored~~ coloured shadings and text boxes indicate each frontal sector. The grey shading on the left represents moisture transport (i.e. ~~IVT~~IVT) that is not considered as AR because it is too weak. The orientation of the x-axis is in flight direction, from west to east.

shows to be little correlated to precipitation formation. Instead, it locally affects the amount of water vapour. To calculate ADV and $CONV$, we use the regression method. Finally, all terms in Eq. 5 are divided by the density of water ρ_w to provide their contributions to the moisture budget (Eq. 2) in ~~$\mathrm{mm\,d^{-1}}$.~~ $\mathrm{mm\,h^{-1}}$.

2.5 ~~Decomposition in~~ AR ~~frontal~~ sectors and sonde locations

~~Current research~~ Research considering IVT divergence in ARs suggests ~~to distinguish~~ distinguishing between different sectors along the lateral AR cross-sections. Guan et al. (2020) highlight that different dynamics take place across the cold-frontal structures that are commonly embedded in the AR, ~~where different dynamics take place.~~ which itself is situated at the western end of warm conveyor belts (Dacre et al., 2019). Hence, Guan et al. (2020) separate IVT divergence calculations across the major AR axis and the AR embedded front. Similarly, ~~using airborne observations of a large set of pacific AR cross-sections,~~ Cobb et al. (2021a) classified different sectors in ARs based on the position of the AR embedded cold front and on the IVT shape of airborne observations of a large set of pacific AR cross-sections. Both approaches distinguish between frontal sectors, namely a pre-frontal (warm) sector, the AR core with highest IVT, near which the cold front is expected (Ralph et al., 2017) , and the post-frontal (cold) sector behind the cold front. Since there exist significant ~~frontal~~ differences in moisture transport divergence between the sectors (Guan et al., 2020), a ~~lot of~~ large part of the variability is smoothed out when calculating IVT divergence for entire cross-sections.

~~Therefore~~Accordingly, we conduct a similar sector-based decomposition of IVT divergence for our arctic AR events in CARRA. As in Guan et al. (2020) and Cobb et al. (2021a), our decomposition relies on the IVT characteristics along the cross-section, which we depict for an ~~exemplary~~ example AR cross-section in Fig. 5. The central AR core represents the region of strongest IVT, which is more than 80 % of maximum IVT (IVT_{max}). ~~East of the core we situate~~ Following Ralph et al. (2017)

, we expect the cold front in the vicinity of the AR core. We denote the region east of the core as the pre-frontal sector ~~and west~~ containing warm air masses, and west of the core as the post-frontal sector that reaches out of the cold front in colder air masses. Since we focus on the AR relevant regions with high IVT, we restrict the outer extents of both extra-frontal sectors. ~~Yet, the outer edges of the frontal sectorsare less trivial as ARs basically have no clear outer boundaries. To account for case-specific relative values~~For both sectors, we assign ~~both frontal~~ the outer edges where $IVT \leq 0.33 \cdot IVT_{\text{max}}$ to account for case-specific relative values (Fig. 5). As a secondary absolute threshold, we declare a moisture transport with $IVT \leq 100\,\text{kg}\,\text{m}^{-1}\,\text{s}^{-1}$ as too weak to be assigned as AR. ~~Both conditions form the outer edges of the AR where the pre- and post-frontal sectors end. Note that the latter~~ This threshold to define the AR edges follows the approach of Cobb et al. (2021a). However, we lower their mid-latitude based IVT threshold from 250 to $100\,\text{kg}\,\text{m}^{-1}\,\text{s}^{-1}$. By this, we refer to common polar moisture transport magnitudes that exceed the 95th percentile of climatology and are declared as ARs in the detection of Guan and Waliser (2015). Otherwise, we would either exclude most ARs north of 70°N or would shrink the AR cross-section so much that most transport is ignored, as the statistics in Fig. 3 indicate. Both thresholds form the outer edges of the AR where our pre- and post-frontal AR sectors end. Note that our sector terminologies only categorise the prevailing air masses of an AR, but should not be viewed as a synoptic cold-frontal identification.

~~Applying the frontal classification to both cross-sections, we obtain three sectors . For the cross-sections~~ Using seven synthetic sondes per cross-section of the AR, we locate the sondes so that ~~six synthetic sondes (three each from~~ three sondes each in the in- and outflow cross-section ~~) span each frontal sector~~ span one out of three frontal sectors (Fig. 6), and calculate its IVT divergence, respectively~~(~~. Given varying sector lengths, the sonde spacing in Fig. 6 ~~). Inspecting the sonde positions~~ is not equidistant. Additionally, the comparison to the IVT contours in Fig. 6 ~~, we emphasise that our~~ reveals that the sondes do not lie at the sector boundaries at the intermediate time step. Our IVT~~-determined frontal AR sectorsalong the flight track tilt while the internal~~ -based AR sectors, i.e. sonde positions, are defined for each airborne cross-section representation individually and thus do not refer to IVT ~~has a straight northward orientation. This arises from the~~ conditions at an instantaneous time step. In fact, there is a north-eastward displacement of the AR filament over the course of the 2.5 h synthetic flight ~~section (Sect. 2.3). Accordingly~~pattern. For this reason, the sectors along the flight track in Fig. 6 tilt while the internal IVT has a northward orientation. Therefore, Sect. 5 examines the extent to which sonde-based IVT divergence is affected by flight duration, as opposed to actually looking at the AR in an instantaneous snapshot.

3 Moisture transport in ~~Arctic~~ arctic AR cross-sections and its variability

~~This section examines the IVT variability in our arctic ARs (Sect. 2.2) using the high-resolution CARRA (Sect. 2.1). First, we analyse the shape of IVT (and document the larger IVT variability compared to forcing ERA5). Next, we focus on the observability of prevailing AR moisture transport variability by discrete soundings, using the synthetic sondes (Sect. ??). We~~ To examine the moisture transport variability in arctic ARs, we follow a two-fold approach. First, we stick to the plane perspective and determine the maximum distance between sondes, needed to derive the total ~~moisture transport~~ IVT in AR cross-sections accurately (Q1). ~~Finally, we describe how coherence~~ The synthetic soundings assess the observability of total

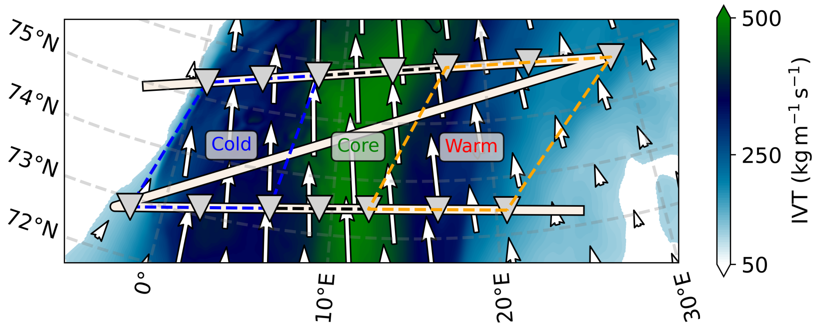

Figure 6. Illustration of AR cross-section sectors and placed sondes to calculate the divergence for AR3AR1. IVT contours refer to CARRA at the hour mid mid-hour of the flight corridor. Dashed lines connect the sonde sectors. Background map made with Natural Earth.

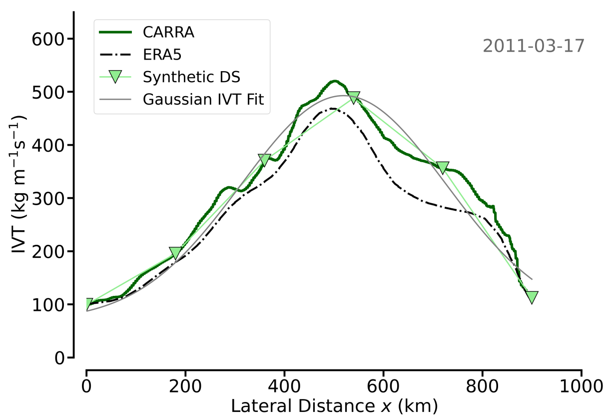

Figure 7. Inflow IVT IVT cross-section from AR1 (2011-03-17) with six synthetic soundings placed along the track. A gaussian Gaussian fit based on the sounding IVT representation is calculated (grey).

moisture transport by discrete sondes. Since we lack real observations, we declare the AR representation in CARRA as our truth. Second, we analyse to what extent coherent patterns in moisture and wind speed contributes anomalies contribute to moisture transport and its variability (Q2). It is crucial to link the results to the large case-to-case variability with respect to IVT magnitude (Fig. 1) and the vertical moisture and wind fields (Fig. 2).

3.1 Shape of IVT shape across arctic ARs

We investigate whether arctic ARs feature the same bell-shaped structure of IVT along their cross-sections as observed in mid-latitudes (Ralph et al., 2017), and to what extent sondes can reproduce the IVT cross-sectionthis structure. For AR1, Figure 7 illustrates the cross-section IVT along the inflow flight leg. We recognise the bell-shaped IVT from both, CARRA and forcing ERA5. Within the cross-section centre which we declare as the AR core in Sect. ??, CARRA , however, 2.5, CARRA shows stronger moisture transport with a more pronounced IVT maximum ($IVT_{\max}$) > $500\,\mathrm{kg\,m^{-1}s^{-1}}$. Moreover, CARRA resolves more small-scale structures of the AR moisture transport. In particular, CARRA increases the cross-section variability for this case.

Summarising all cross-sections of our ARs from Sect. 2.2, most arctic AR cross-sections show this typical bell-shaped IVT curve over widths of roughly 400–800 km and indicate pronounced IVT maxima ~~in the core~~ of 300–600 $\mathrm{kg\,m^{-1}s^{-1}}$ in the core (not shown). ~~Only for the weak AR8, this structure is less pronounced.~~ We find that the arctic ARs are not substantially narrower than the AR widths of global climatology (Guan and Waliser, 2015) and observed mid-latitudes events (Cobb et al., 2021a). Flight planning should therefore consider cross-section distances of about 500-1000 km, similar to mid-latitude ARs. However, this only applies if the legs are not restricted to regions with $IVT > 250\,\mathrm{kg\,m^{-1}s^{-1}}$ which is a widely used threshold for mid-latitude ARs (e. g. Ralph et al., 2019). In contrast, the maximum IVT for the arctic events is roughly half as high as the majority of mid-latitude ARs from airborne studies in Cobb et al. (2021a). Moreover, the IVT magnitudes strongly differ between our cases and synoptic conditions. The strongest ARs, with $IVT_{\max}$ exceeding $500\,\mathrm{kg\,m^{-1}s^{-1}}$ are found for intense Greenland troughs, while the ARs are weaker along the Siberian pathway (see also Fig. 1). ~~If we compare our ARs with those of~~ In comparison to other arctic case studies (e. g. Viceto et al., 2022), we ~~are looking at rather strong ARs~~consider rather strong ARs.

Viceto et al. (2022) documented the improved representation of arctic AR characteristics in ERA5 against coarser reanalysis data. In our comparison of CARRA with ERA5, the location and horizontal patterns of the ARs agree quite well (not shown). For all cross-sections, we ascertain plausible IVT values from CARRA with respect to ERA5. ~~In particular, we~~ We highlight that maximum (mean) values of IVT per cross-section increase by roughly 9 % (8 %) from ERA5 to CARRA on average. CARRA ~~further increases the~~ thus increases IVT variability by ~~roughly~~ around 11 %. We attribute this to the higher horizontal resolution ~~than in ERA5~~of CARRA. The increased IVT variability supports our treatment of CARRA as ground truth, before dedicated observations will be conducted.

Using a set of six synthetic sondes, a ~~gaussian~~ Gaussian fit of IVT can reproduce the bell-shaped AR-IVT cross-section (Fig. 7). ~~This gaussian~~ However, the Gaussian fit is very sensitive to the actual positions of dropsonde releases. While the centred sonde in Fig. 7 is positioned close to $IVT_{\max}$, a slight shift of this sounding, which easily occurs in real observations, can quickly lead to an underestimation of the moisture transport in the AR core. Flight planning should thus imply a sonde release in the vicinity of the predicted IVT maximum and place additional sondes symmetrically around the core. ~~While sonde positions in Fig. 7 are suitable to represent the cross-section IVT, other AR cross-sections evince more complexity in being accurately represented by this number of soundings. We need further inspections on how sounding intervals deteriorate the AR moisture transport observability.~~

3.2 Sonde-based total cross-section moisture transport

~~As stated in Sect. **??**, the determination of $TIVT$ in two AR cross-sections can provide first estimates on the prevailing IVT divergence. However, the~~ The accuracy in sonde-based $TIVT$ of an AR cross-section depends on the number of sondes across the AR, i.e. their spacing (Ralph et al., 2017). ~~For AR1, one of~~ Larger spacing of sondes affects the derived total moisture transport of AR cross-sections, whereby the sonde location becomes increasingly relevant. For example, the stronger events with $IVT_{\text{max}} \approx 500\,\text{kg}\,\text{m}^{-1}\text{s}^{-1}$ (presented in Fig. 7), we find that from the release equidistant placing of six sondes we underestimate within AR1, as shown in Fig. 7, underestimates $TIVT$ by roughly 10 % against the continuous IVT representation in CARRA (defined in Sect. ??). In contrast, $TIVT$ estimates based on ten sondes differ by less than 1 % (not shown). . For all of our AR events, ARs, we assess the required sounding spacingsounding spacing, needed to gain adequate $TIVT$ estimates, by varying the frequency between density of synthetic sondes and by comparing their values with $TIVT$ $TIVT$ values with those of the continuous AR cross-section representation in CARRA. When increasing the spacing between soundings, their location becomes more essential and strongly affects the derived moisture transport variability. Relative error in $TIVT$ as a function of sounding spacing in km for all AR cross-section representations (grey) and those including highest (75th percentile) IVT maxima (coloured). Statistics rely on the boots-trapping approach containing of 100 cross-section sonde representations per AR. The boxes show the quartiles while whiskers show the rest of the distribution, except for outliers (markers). For an assumed aircraft speed of 250 m s^{-1}, equivalent release intervals are given on the top x-axis. To account for this dependency , Figure 8 illustrates the outcome of the dependency on sounding location, we conduct a bootstrapping approach in which we sample the cross-sections with varying release intervals and varying positions and derive $TIVT$ therefrom. The distributions of the relative error of $TIVT$ against the continuous AR representation (spacings and varying sounding locations. From this, the grey box-whiskers in Fig. 8) reveal how dense sonde releases need to be performed in order to derive $TIVT$ in the AR cross-sections precisely. Correspondingly, , showing the distribution of sonde-based errors of $TIVT$, reveal that the relative error of $TIVT$ against the continuous AR representation increases significantly for sounding spacing $\geq$ 150 km(. This corresponds to roughly five sondes for the given cross-section lengths, corresponding to and release intervals above 10 min at a cruising speed of 250 m s^{-1})). For sonde spacing $\geq$ 200 km, sonde-based $TIVT$ can substantially deviate.

The $TIVT$ uncertainty in Fig. 8 increases less rapidly with larger sonde spacing than derived for mid-latitude AR cases (see Ralph et al., 2017 and Guan et al., 2018). Total moisture transport in the arctic cases is, in turn, much smaller than in mid-latitude cases. The Our arctic $TIVT$ values are roughly half as high as the sonde-based mean $TIVT$ of $5{\cdot}10^{8}\,\text{kg}\,\text{s}^{-1}$ ascertained by Ralph et al. (2017) from 21 mid-latitude ARs. The ARs we consider have , in turn, Our ARs have roughly two third the width of the ARs in Ralph et al. (2017) and Guan et al. (2018). HereStill, we remind that our threshold to define the outer AR edges IVT threshold, scaling the outer edges of the AR, is much lowerto encounter for arctic AR conditions. Applying the . Using mid-latitude thresholds (given in Sect. ??based thresholds (Sect. 2.5), mean AR widths would be in the range of a few hundred kilometer kilometres and $TIVT$values much lowerthan in mid-latitude ARss even lower.

With increasing spacing, the spread in $TIVT$ errors in Fig. 8 increases. One reason is , mainly due to the rising relevance of the sonde position. Too large sonde spacing enhances the probability to miss likelihood that the sampling will not capture the region of strongest IVTdominating regions. Especially with the occurrence of a LLJ, Guan and Waliser (2017) confirm that the AR corealone , alone, accounts for $\approx 50\,\%$ of the entire moisture transportthrough the cross-section. Yet, we also attribute the spread in relative $TIVT$ errors to the large AR case-to-case variability in maximum IVT. In particular, the strong correlation of IVT_{max} to IVT variability (correlation coefficient $r = 0.91$) may cause sonde errors in derived $TIVT$. Hence, we expect that the smallest sonde spacing is required for the strongest AR events. However, The coloured box-whiskers in Fig.

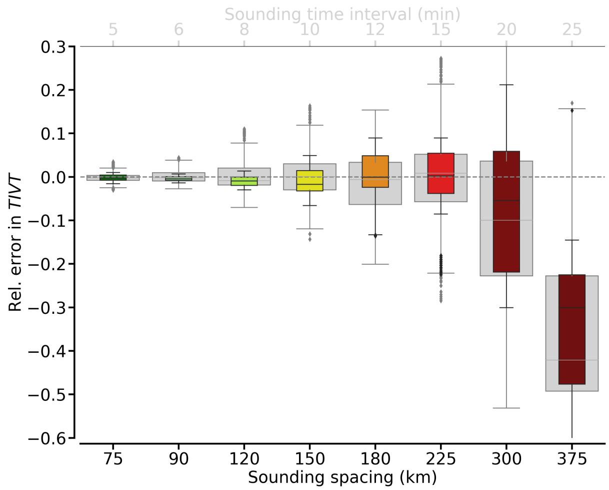

Figure 8. Relative error in $TIVT$ as a function of sounding spacing in km for all AR cross-section representations (grey) and those including highest (75th percentile) IVT maxima (coloured). Statistics rely on the boots-trapping approach, containing of 100 cross-section sonde representations per AR. The boxes show the quartiles, while the whiskers show the rest of the distribution, except for outliers (markers). For an assumed aircraft speed of 250 m s^{-1}, equivalent release intervals are given on the top x-axis.

8 show that the distribution of the relative $TIVT$ error behaves similarly, when we ~~refer to the cross-sections~~ only include the cross-section representations with IVT_{max} larger than the 75th percentile from the bootstrapping sample~~, mainly from AR1 and AR3 (coloured box-whiskers in Fig. 8)~~. The mean relative error increases more rapidly with ~~larger spacingwhereas~~ spacing, while the inter-case spread is slightly lower than in the entire sample. ~~For sonde spacing $\geq$ 200 km, the mean error becomes slightly lower than in the entirety but more robust.~~

We conclude that highest $TIVT$ errors thus do not originate from the ~~strong~~ strongest events when having very few sondes. Still, we ~~emphasis~~ emphasise that a minimum sounding spacing of 100-150 km has to be targeted for arctic ARs, which is less restrictive than for mid-latitude ~~ARs~~ ARs in Ralph et al. (2017). ~~In a larger set of arctic AR events than in this study, these recommendations for sonde spacing could be further specified in terms of arctic AR strength.~~

3.3 Variability of moisture and wind in arctic ARs

~~After investigating the overall moisture transport by its vertical integral IVT, we take a deeper look at moisture q and wind speed v (Eq. 1) individually in order to address Q2 (Sect. 1). For all arctic ARs, Figure 9examines~~ To address (Q2), Fig. 9a,b) summarise the cross-section variability of v and q over the vertical profile ~~using the continuous AR representation (Sect. ??). Here, moisture~~ for all arctic ARs. Moisture transport in the lowest levels up to 850 hPa ~~contains roughly~~ is most effective and accounts for 50 % of the total IVT ~~magnitude~~(Fig. 9c). Up to this height, both high moisture and wind speeds are predominant, with a local maximum of wind speeds around 900 hPa. Further upwards, wind speed accelerates up to ~~20–30~~20–40 m s^{-1} while the atmosphere dries with height. The ~~height decreasing moisture~~ drying with height leads to a decline of moisture transport.

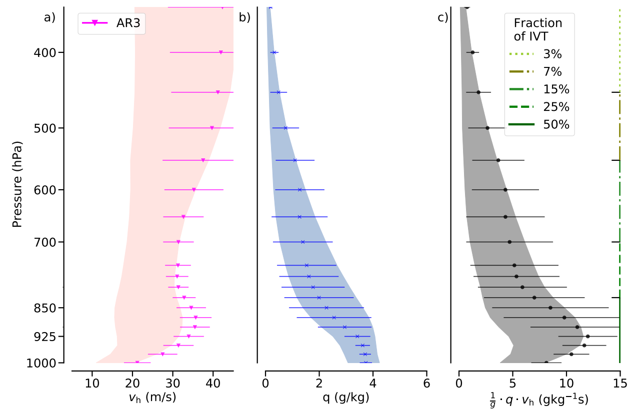

Figure 9. Vertical statistics of wind speed (a), specific humidity (b) and moisture transport (c) from the inflow cross-sections of the nine ARs analysed. Shaded areas represent the overall mean values $\pm$ the standard deviation. The error bars depict this distribution for the strongest AR (AR3). Vertical lines in c) specify the cumulative contribution of moisture transport to IVT down to the given levels.

Through the entire troposphere, q ~~overall remains~~ is always below $5\,\mathrm{g\,kg^{-1}}$ in our arctic ARs. The vertical moisture characteristics ~~in~~ (Fig. 9b) ~~resemble~~ agree with the study by Viceto et al. (2022) who documented q values up to $5\,\mathrm{g\,kg^{-1}}$ in soundings of arctic early summer ARs at Ny-Alesund~~demonstrated in Viceto et al. (2022) who showed q values up to $5\,\mathrm{g\,kg^{-1}}$~~. However, the winds in our AR cross-sections (Fig. 9a) are roughly twice as strong as ~~given in the case studyof Viceto et al. (2022). Note that the ground-based station from which Viceto et al. (2022) depicted soundings were basically located at the outflow edge of the AR (with $IVT \leq 250\,\mathrm{kgm^{-1}s^{-1}}$) on the Luv side. Winds from the east were orographically slowed down by the massif of Svalbard. In this sense, the marine arctic ARswe consider are undisturbed. This~~ in their case study, which reports an orographic deceleration by Svalbard. For our arctic ARs, the open ocean enables stronger winds~~whose magnitude is~~, rather comparable to the wind conditions in the mid-latitude ~~AR conditions .~~ ARs. There, Ralph et al. (2004) and Cobb et al. (2021b) report on mean low-level wind speeds from 10–25 $\mathrm{m\,s^{-1}}$ for a large set of ARs over North-East Pacific. The slight local wind maximum at 900 hPa (Fig. 9a) arises from the presence of ~~strong wind corridors designated as LLJs that represent a common feature in mid-latitude ARs (Ralph et al., 2004; Demirdjian et al., 2020). Their polar existence is verified in the case study of Terpstra et al. (2021). We find a very dominant LLJ inside our most intense AR (AR3 in Fig. 9~~LLJs (see also Fig. 2). Above the local wind maximum, the vertical profile of wind speed remains more homogeneous than in sub-tropic/mid-latitude cases~~where~~, in which Ralph et al. (2005) and Cobb et al. (2021a) registered a stronger intensification with height.

The cross-section variability of both moisture and winds strongly affects ~~IVT~~ moisture transport variability. The shadings in Fig. 9c) indicate that the horizontal standard deviation of moisture transport resembles the standard deviation of the winds for the lower levels up to 850 hPa~~, before~~. At higher levels, moisture transport variability is ~~apparently~~ driven by the standard deviation of moisture~~in upper levels, although~~, and the intrusion of dry airmasses on the western flank (see Fig. 2), even though the wind standard deviation becomes highest above 500 hPa. ~~For the most intense AR~~ For example, in the strongest AR (AR3;

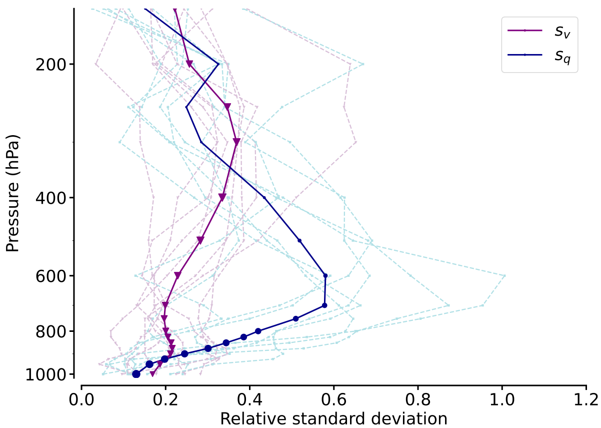

Figure 10. Vertical profile of relative standard deviation of wind (s_v) and moisture (s_q) for the AR cross-sections of each flight. The bold lines indicate the mean value over all ARs for both components. The sizes of the dots ~~scale with~~ are scaled by the mean value at this height normed by the maximum mean value for the entire profile.

Fig. 9), the LLJ exhibits high wind speeds above $30\,\mathrm{m\,s^{-1}}$ that cause strong moisture transport, whereas moisture is more or less average~~(Fig. 9a)~~. While strong moisture transport in AR3 originates from overall strong winds, moisture varies strongly and seemingly dominates the moisture transport variability (Fig. 9b). Hence, we hypothesise that in strong arctic ARs with intense winds, moisture variability primarily steers IVT variability and leads to the bell-shaped IVT cross-section pattern depicted in Sect. 3.1.

The identification of the more variable quantity can improve measurement strategies. Specifically, ~~moisture can be derived from~~ in case of a moisture dominance, the ability of supplementary remote sensing devices ~~on long-range research aircraft . For this reason~~from the research aircraft to derive moisture fields could be explored. To this end, we quantify the relative standard deviations of wind and moisture (s_q and s_v), normalised by the horizontal mean. We investigate s_q and s_v as a function of height (Fig. 10). Especially for the winds, the relative standard deviation in Fig. 10 remains rather ~~consistent~~ constant throughout the troposphere and has a small magnitude ~~(mean relative variability around~~ of 20 to 35 %~~). This is in accordance with the high but rather homogeneous wind speeds in AR3 (Fig. 9)~~. Besides a weak local maximum in the vicinity of the LLJ, the variability increases slightly near the upper-level polar jet, but with minor impact on the moisture transport (variability) due to dry air masses. Correspondingly, the wind contours of Fig. 2 indicate stronger horizontal gradients above 500 hPa, while moisture transport is already minor.

The variability of moisture behaves differently. In the boundary layer, moisture variability is negligible, similar to wind ($s_q, s_v < 20\,\%$). Yet, the decline of mean moisture with height is opposed by an increase of its relative variability. Between 600 and 850 hPa, high moisture variability ~~, increasing half as high as its mean, basically contributes~~ (s_q up to 50 % and more) contributes significantly to mean moisture transport variability. Based on our AR cross-sections, we conclude that moisture represents the more variable quantity in arctic ARs, which was already indicated in Fig. 2 by the prominent moisture plumes.

3.4 Coherence of moisture and wind

For the moisture transport, it is not ~~only~~ merely important whether moisture and wind anomalies ~~are high~~ exist separately (Sect. 3.3), but also how correlated they evolve along the AR cross-sections and whether ~~connected~~ such coherent patterns contribute significantly to AR-IVT (Q2). If both patterns ~~do~~are coherent, carefully collocated observations are essential to determine $TIVT$, otherwise independent estimates of mean moisture and wind are sufficient. ~~The~~ Therefore, we decompose the overall moisture transport $\overline{q \cdot v}$ ~~is basically~~ that basically is a combination of transport by the mean quantities $\overline{q}$ and $\overline{v}$ and their ~~correlated~~ cross-section variability, i.e. the spatial fluctuations q' and v', according to:

$$\overline{q \cdot v} = \overline{(\overline{q}+q')(\overline{v}+v')} = \overline{q} \cdot \overline{v} + \underbrace{\overline{q'\overline{v}}}_{=0} + \underbrace{\overline{\overline{q}v'}}_{=0} + \underbrace{\overline{q' \cdot v'}}_{\mathrm{cov}(q,v)} . \quad (6)$$

While the second and third summand equal zero, the last term represents the covariance cov() between q and v. Using the relation between correlation coefficient r_{corr} and cov(), we obtain:

$$\mathrm{cov}(q,v) = r_{\text{corr}}(q,v) \cdot \mathrm{std}(q) \cdot \mathrm{std(v)}, \quad (7)$$

and expanding by $\overline{q}$ and $\overline{v}$, we can reformulate Eq. 6 as:

$$\overline{q \cdot v} = \overline{q} \cdot \overline{v} \cdot (\underline{1+}\underbrace{r_{\text{corr}}(q,v) \cdot \underbrace{\frac{\mathrm{std}(q)}{\overline{q}}}_{s_q} \cdot \underbrace{\frac{\mathrm{std}(v)}{\overline{v}}}_{s_v}}_{cov_{\text{norm}}} +1). \quad (8)$$

The normalised covariance cov_{norm} (~~right~~ left summand in Eq. 8) weighs the coherent transport by fluctuations relative to the non-coherent $\overline{q} \cdot \overline{v}$. Using cov_{norm}, ~~Figure~~ Fig. 11 finds rather little coherence between moisture and wind in arctic AR cross-sections. The magnitude of the contribution of moisture transport variability to the overall moisture transport is below $\pm 10\,\%$ for each height. Accordingly, the coherence is of minor influence for the entire IVT variability. Main reasons for the low contribution of coherent patterns are the relatively low standard deviations compared to their mean (see s_q and especially s_v). Even considerable correlation ($r_{\text{corr}} \geq 0.5$, Fig. 11) cannot generate relevant moisture transport contributions. Over the vertical extension, cov_{norm} mostly remains below 5 %. Even ~~in moisture transport dominated levels (below 700 hPa),~~ for low levels that contain most of the moisture transport (≥ 700 hPa), where considerable correlation of q and v is predominant, the cross-sections reveal a contribution of moisture transport variability to Eq. 8 in the range of 5 to 10 %. ~~Only for some ARs, the strongest variability~~ Here, q and v prevail with high values, but weak horizontal gradients (see Fig. 2). The strongest covariance ($> \pm 10\,\%$ ~~) primarily~~ for a few ARs) mainly occurs in higher levels above 500 hPa, where ~~, in turn,~~ moisture transport is weak (Fig. 9 and ~~Fig.~~ 11).

~~The~~ In contrast to cov_{norm}, the correlation between moisture and wind r_{corr} shows a large spread between the single ARs (grey lines in Fig. 11)~~, so that we take a closer look into the spatial patterns of moisture and wind for our AR cross-sections in Figure 2. Inspecting the vertical AR curtains in Fig. 2, we recognise several features that we know from mid-latitude ARs. For instance, Ralph et al. (2004) and Cordeira et al. (2013) found the vertical slanted structure of moisture transport in AR cross-sections~~

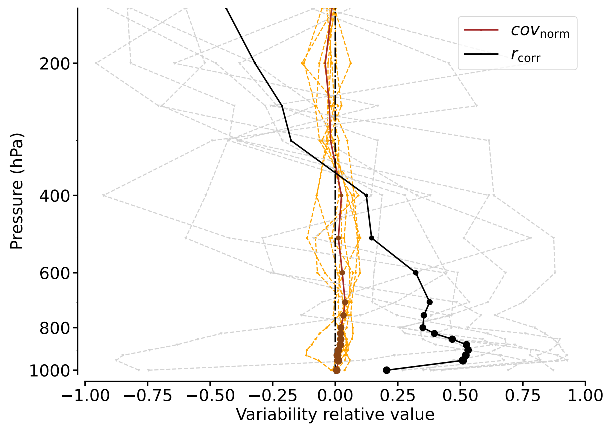

Figure 11. Vertical profile of AR moisture and wind normalised covariance (cov_{norm}) and their correlation r_{corr} along the cross-sections. The bold lines indicate the mean value over all AR for each of the components. The sizes of the dots scales with the mean moisture transport value at this height normed by the maximum mean value of the entire profile.

from dropsondes and reanalyses, where Ralph et al. (2017) verified the vertical interaction between the upper-level jet and the LLJ that dominates the AR moisture transport. In . Apart from AR5, other ARs exhibit less coherent patterns where wind and moisture do not necessarily correlate with each other (see also Fig. 2, their conceptual depictions reflect mostly for AR5). Valid for most of the ARs, the correlation between moisture and AR6 where moisture and wind are most coherent. Here, moist air masses residing in the warm conveyor belt are lifted over the cold-frontal sector. The downward intrusion of the upper-level jet on the eastern flank causes the slanted structure in the moisture transport. For the windy arctic AR events, e.g. AR3 and AR5, we detect the presence of LLJs stronger than $25\,\mathrm{m\,s^{-1}}$. The LLJ is situated at a heightof around 900 hPa, slightly lower than Cobb et al. (2021a) summarised for mid-latitude ARs. In almost every cross-section (Fig. 2), the specific humidity exceeds $4\,\mathrm{g\,kg^{-1}}$ indicating that our events are rather moist for arctic AR conditions (e.g. Viceto et al., 2022), but much drier than mid-latitude ARs where q easily exceeds $8\,\mathrm{g\,kg^{-1}}$ (Cobb et al., 2021a). Still, we notice a large case-to-case variability wind peaks in the LLJ height. The low-level negative correlation in Fig. 2 and partially less compliance to the conceptualised AR schematics illustrated in Ralph et al. (2017). This shows for the vertical structure of moisture, the presence and intensity of the LLJ (strongly distinctive in AR1, AR3, AR5, AR7, but missing in the other ARs) and how patterns of moisture and wind are correlated. Apart from AR5, other ARs exhibit less coherent patterns where 11 refers to AR9, indicating a clear horizontal displacement of the wind and moisture do not necessarily align with each other. Especially AR9 indicates a clear horizontal displacement, causing a negative correlation along the cross-sectionfields (Fig. 2). Here, subsiding dry air masses in the cold sector counteract the westward increase of wind speeds. For all ARs except for AR1, AR8 and AR9, the correlation between moisture and wind peaks in the LLJ height ($r_{\mathrm{corr}} > 0.7$,

Summarizing Fig. 10 and Fig. 11, the moisture variability mainly steers the moisture transport variability above the marine boundary layer. This shows analogously in more horizontal overlap between fields of moisture and moisture transport as against the wind fields (Fig. 2). Especially, AR1 and AR3 exhibit small horizontal variability in the wind field, as winds are almost constant along the entire cross-section ($> 25\,\mathrm{m\,s^{-1}}$). ~~Here, it is the moisture variability steering the moisture transport variability. The~~ ARs, being variable in moisture, consist of an elevated moist plume only residing in the AR core that is surrounded by dry air. The ~~strength of dry air subsidence is primarily relevant for slanting the moisture transport along the cross-section. We find this most effective for ARs close to the dry air masses east of the Greenland coast (AR3)and when the backside of the embedded cyclone advects the dry Greenland air masses (AR9). The variety of moisture transport characteristics comes with the very different synoptic patterns (troughs, ridges, smaller cyclones embedded in a meridional, but rather weak flow) causing the arctic ARs. In addition, we consider different corridors~~ extension and intensity of the moisture plume in the mid-levels mainly controls the moisture transport variability (Fig. 10), while the location controls the case-to-case variability in the correlation of moisture and winds. The case-to-case variability in wind and moisture fields is also aligned with partly different regions of the respective ARs that we consider. While AR5 was mainly observed in the AR ~~center~~centre, other ARs such as AR2-4 and AR7 are ~~observed~~ sampled in the exit region of the AR (see Fig.1 and Fig. 3). Terpstra et al. (2021) detected that moisture and wind patterns and their coherence in polar ARs strongly change along the AR direction. In their case study, the pronounced AR pattern, as depicted in Ralph et al. (2017), vanishes out more towards the Poles and the AR exit region. ~~Similarly, the most textbook AR among our cases, AR5, is also the southernmost AR (Fig. 1).~~ Moreover, Terpstra et al. (2021) identified decreasing coincidence between moisture and wind in the polar AR exit region. ~~In their case, the~~ Their LLJ resides in rather dry regimes below the local moisture maximum. ~~While we~~ We detect this vertical separation of moisture and wind patterns mainly for AR4, but less uplifting of maximum moisture~~than in Terpstra et al. (2021)~~. In turn, we emphasise the horizontal displacement of moisture and wind sectors in AR exit corridors~~(Fig. 2)~~, such as for AR9, that causes the decorrelated low-level profile in Fig. 11.

~~Cross-sections of AR inflow legs for moisture (color-coded contours), as well as wind contour lines for (pinkish) and moisture transport (both as contour lines). Shown moisture transport values have the unit $\mathrm{gkg^{-1}ms^{-1}}$. The black-white dashed vertical line represents the cross-sectoral mean of the correlation coefficient r_{corr} between moisture and wind for each pressure level. We conclude that~~ In conclusion, the mean moisture and wind account for 95 % of overall moisture transport in arctic ARs. Moisture and wind patterns exhibit little coherence, especially in arctic AR exit corridors, but show high ~~inter-case variability . Despite the variability, we postulate~~ case-to-case variability in their correlation. We find that strong ARs ($IVT \geq 400\,\mathrm{kg\,m^{-1}s^{-1}}$) tend to feature strong, but rather constant winds. Instead, narrow and high-reaching moisture plumes in the core control the AR moisture transport variability~~. The effectiveness~~ , and the intensity of dry subsidence ~~backwards the AR modulates the AR moisture transport pattern~~on the western AR flank further modulates moisture transport variability. An improvement for observing the moisture transport variability should thus be built upon supplementary moisture measurements rather than those of ~~the winds. Incoherent~~ winds.

4 Moisture transport divergence from sondes

The incoherent cross-section patterns ~~motivate investigating separate sectors along the AR front as they exhibit different processes (Cobb et al., 2021a). When~~ of moisture and wind ~~patterns do not coincide, we can expect cross-frontal~~ fields (Sect. 3) suggest lateral differences in the moisture transport divergence components (Eq. 5) ~~.~~

5 ~~Moisture transport divergence from sondes~~

~~This section analyses how the divergence of moisture transport is characterised along cross-sections of arctic ARs (Q3). Resuming the decomposed terms (Eq. 5), we inspect~~ and motivate investigating the divergence in separate sectors across the front embedded in the AR. Showing the limits in $TIVT$-based divergence, we investigate whether high moisture advection occurs more frequently in strong moisture-dominated AR sectors and whether mass convergence dominates in windy AR sectors. ~~We categorise~~ By categorising our results based on ~~frontal sectors defined in Sect. **??**. Synthetic sondes illuminate how discrete soundings reflect such characteristics against the continuous flight representation along the AR cross-sections~~ the AR sectors (Sect. ~~**??**).~~ 2.5), we examine how the divergence of moisture transport is characterised along cross-sections of arctic ARs (Q3), and evaluate how the sondes reproduce the features of the continuous cross-section representation.

4.1 In- and outflow IVT

~~Before coming to the moisture transport divergence at single levels, we compare the integrated quantities, namely cross-section IVT of the in- and outflow leg and their AR-$TIVT$ for all nine arctic ARs (Fig. 12). The comparison of $TIVT$ in both legs reveals first simplified estimates of the prevailing divergence. Idealising that no entrainment into the AR corridor (Sect. 3) takes place, Figure 12 contrasts $TIVT$ of the in- and outflow cross-section to estimate whether convergence or divergence of moisture transport inside the AR corridor exists. Figure 12 indicates that~~ The IVT cross-sections show maximum IVT values ~~vary~~ varying between 200–650 $\mathrm{kg\,m^{-1}s^{-1}}$ ~~, with~~ for all ARs, while the outflow IVT generally ~~having~~ has a similar intensity to the inflow leg (Fig. 12). The strongest AR in terms of maximum IVT ~~also~~ has the highest total transport in both flight legs. Overall, $TIVT$ ~~overall~~ ranges from $100–300 \cdot 10^6\,\mathrm{kg\,s^{-1}}$. Recall that this is approximately one third to one half the $TIVT$ magnitude found in mid-latitude ARs (Ralph et al., 2017). ~~Figure 12 further separates the AR cross-sections in the three sectors (pre-frontal, core, post-frontal).~~ Although the AR cores are roughly 200–300 km ~~narrow (slim lines in Fig. 12)~~wide, they provide more than half of the entire ~~AR-~~$TIVT$. This contribution of the AR core agrees with findings from Cobb et al. (2021a) in mid-latitude ARs. Except for AR2 and AR7, weaker slopes of IVT are generally in the cold sector as opposed to the warm sector. ~~In turn, the~~ The steep post-frontal IVT decline in AR2 and AR7 results from calm air masses ~~on the backside~~ west of the AR (~~see also~~ Fig. 2). ~~Comparing both~~

By contrasting the in- and outflow cross-section legs (Fig. 12), ~~cross-section~~ it can be estimated whether convergence or divergence of moisture transport inside the AR corridor exists, under the idealisation that no lateral entrainment into the AR corridor occurs (Sect. 2.4). However, we emphasize that a $TIVT$~~tends to decrease downstream in some arctic ARs. Here, higher~~ -based interpretation of predominant moisture transport divergence underlies strong idealisation. It neither

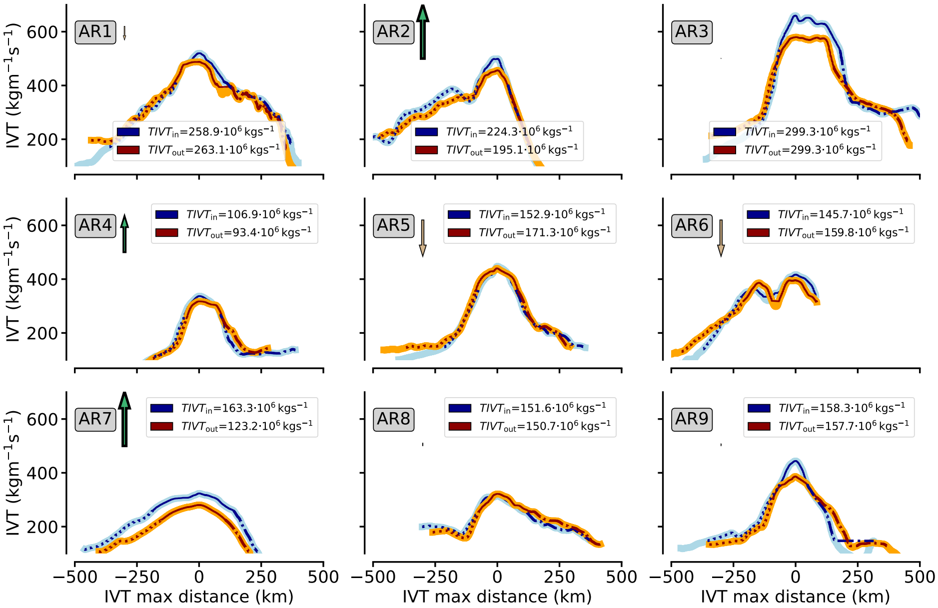

IVT along inflow (outflow) legs in blue (orange) for all nine ARs (Fig. 1). Changes in line styles denote the frontal sector classifications (Sect. ??): Dotted lines represent cross-section periods attributed to pre-frontal sectors, while dashed lines refer to post-frontal sectors. The legend depicts $TIVT$ values for the in- and outflow cross-section parts within the AR. They include IVT purely internal of determined AR borders (Sect. ??). Arrows indicate the $TIVT$ difference between in- and outflow leg scaled in length and width. The differences can be viewed as simple estimates of IVT divergence in between both legs, according to Sect. 2.4. Upward (downward) arrow scales represent estimated convergence (divergence) magnitudes. Note the x-axis orientation is from east (left) to west (right).

Figure 12. IVT along inflow (outflow) legs in blue (orange) for all nine ARs (Fig. 1). Changes in line styles denote the AR sector classification (Sect. 2.5): Dotted lines represent cross-section parts attributed to pre-frontal (warm) sectors, while dashed lines refer to post-frontal (cold) sectors. Legend values depict $TIVT$ for the in- and outflow cross-section parts within the AR. They include IVT purely internal of determined AR borders (Sect. 2.5). Arrows indicate the $TIVT$ difference between in- and outflow leg, scaled in length and width. The differences can be viewed as simple estimates of IVT divergence in between both legs, according to Sect. 2.4. Upward (downward) arrow scales represent estimated convergence (divergence) magnitudes. Note the x-axis orientation is from east (left) to west (right).

considers moisture flow being non-perpendicular to the flight and from the western and eastern boundaries, nor does it separate contributions of moisture advection and mass convergence.

When looking more closely into different aspects of IVT and $TIVT$ in the inflow leg suggests potential convergencein the AR corridorvalues along the ARs, several effects that might cancel each other out become more apparent. In some cases, IVT and $TIVT$ values across the AR decrease downstream, suggesting convergence. Yet, we likewise identify cases with weak stream-ward tendencies in total moisture transport or with slight increases, suggesting divergence (AR5 and AR6). Moreover, the downstream difference of $TIVT$ is unevenly distributed over along the cross-section IVT. It is mainly within , and mainly occurring at the AR core where IVT decreases towards the outflow leg (e.g. AR3, AR9), thus here suggesting internal convergence. However, counteracting ~~behavior~~ behaviour in the frontal sectors partially compensates the core and stream-ward decrease of IVT ~~. Like in~~ (e.g. suggesting pre-frontal divergence in AR5 and AR6~~, the increase of warm sector IVT towards the outflow conveys a seeming divergence. This~~). This potential divergence is in contrast to the findings in Guan et al. (2020), where the pre-frontal sector is denoted as a region of moisture transport convergence. ~~Nonetheless, although the IVT patterns of AR5 and AR6 (Fig. 1) allow slight divergence in the pre-frontal sector, we emphasize that a $TIVT$-based interpretation of predominant moisture transport divergence underlies strong idealisation. It considers neither moisture flow being non-perpendicular to the flight, nor does it separate contributions of moisture advection and mass convergence.~~ Therefore, we ~~insist~~ decide on the regression approach from Sect. 2.4 to diagnose moisture transport divergence in each frontal sector of the arctic ARs, and to avoid strong idealisation of the exclusively $TIVT$-based interpretation.

4.2 Sonde-based divergence and its representativeness

~~This section derives~~ To derive the IVT divergence (∇IVT)~~in arctic ARs. Using~~ , we thus use the regression-based approach (Sect. 2.4) ~~. The moisture transport divergence is specified for the frontal sectors (Sect. **??**) and for the decomposed terms, namely~~ for moisture advection ADV and mass convergence $CONV$ (Eq. 5). ~~Again, the~~ The results from the continuous ~~cross-section flight legs (Sect. **??**) represent our idealised reference. We compare them to the results referring to seven synthetic sondes per cross-section (as~~ cross-sections are compared to results based on the synthetic sondes that sample the cross-sections (as illustrated in Fig. 6). ~~This comparison assesses uncertainties of sonde-based ∇IVT, representative for arctic AR conditions. In doing so, we build on Norris et al. (2020) who pioneered the airborne derivation of all AR moisture budget components, including moisture transport divergence, by sampling a mid-latitude AR event. Vertical contributions from ADV (a) and $CONV$ (b) to moisture transport divergence (c) for the frontal sectors in AR3. Bold lines represent the continuous AR representation while dashed lines depict the sonde-based representation with the deviations as shadings. In a first step, Figure 13 delineates the divergence components for the frontal sectors within the intense AR3.~~

In the continuous ~~AR~~ representation, ADV and $CONV$ exhibit different vertical profiles throughout the ~~frontal~~ cross-section ~~(Fig. 13). Comparing~~ AR sectors. For the intense AR3, moisture transport divergence values in the sectors ~~for the continuous representation, we see that values range from −3~~ range from $-3 \cdot 10^{-4}$ to $+1 \cdot 10^{-4}\,\mathrm{g\,kg^{-1}s^{-1}}$ (Fig. 13). While moisture advection (ADV) does not rise above ~~$\pm 1 \cdot 10^{-4}\,\mathrm{g\,kg^{-1}s^{-1}}$~~ $\pm 1 \cdot 10^{-4}\,\mathrm{g\,kg^{-1}\,s^{-1}}$, mass divergence ($CONV$) decreases below~~$-2 \cdot 10^{-4}\,\mathrm{g\,kg^{-1}s^{-1}}$. For AR3, the~~ $-2 \cdot 10^{-4}\,\mathrm{g\,kg^{-1}s^{-1}}$. The post-frontal sector is most crucial for moisture transport divergence. In detail, substantial advection occurs in the post-frontal cold sector, whereas the warm pre-frontal sector and the core exhibit weak advection (Fig. 13a)~~, whereas substantial advection occurs in the post-frontal cold sector~~. Similarly, the strongest mass convergence is found ~~for~~ within the post-frontal sector (Fig. 13). Not only ADV and $CONV$ act differently between the frontal sectors, they also dominate in different vertical levels. The maxima of ADV and $CONV$ locate at the heights where ~~also~~ moisture and wind dominate (Fig. 2). While advection is predominant at mid-levels above 800 hPa up to 500 hPa, the mass divergence primarily acts below this level (Fig. 13 a~~and~~ , b). In the vicinity of the LLJ in the AR core at around 850 hPa, predominant mass convergence (negative values) prevails, although the vertical column is slightly divergent in total. The advection of moisture in the prefrontal sector and core is too weak (Fig. 13a) to compensate the more prominent

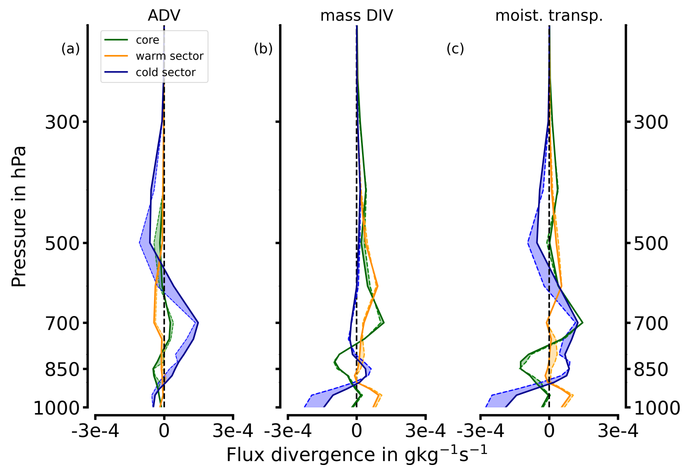

Figure 13. Vertical contributions from ADV (a) and $CONV$ (b) to moisture transport divergence (c) for the frontal sectors in AR3. Bold lines represent the continuous AR representation, while dashed lines depict the sonde-based representation with the deviations as shadings.

mass divergence (Fig. 13b). Overall, the moisture transport convergence (divergence) dominates in the cold post-frontal (warm pre-frontal) sector of AR3 (Fig. 13). We attribute the drying in mid-levels of the cold sector in AR3 to the dry cold air masses overrunning the AR behind the cold front (as also visible in Fig. 2c). The change in IVT direction behind the cold front ~~(see Fig. 6)~~ accounts for the low-level mass convergence in the post-frontal sector (not shown).

The fact that the moisture transport divergence components differ across the frontal axis is in line with mid-latitude AR based statistics of Guan et al. (2020). In detail, the characteristics in AR3~~described above differ quietly to~~ , described above, differ from the AR case observed by Norris et al. (2020). In their airborne study of a mid-latitude AR, they found moisture transport convergence to be strongest close to the AR core and found rather opposite signs for the pre- and post-frontal regions ~~than us. Especially the lack~~ to us. It is worth mentioning the weakness of pre-frontal moisture advection in AR3, ~~which Guan et al. (2020) actually robustly found~~ while advection is more enhanced in mid-latitude AR statistics ~~, is worth-mentioning~~(Guan et al., 2020). In contrast to both Norris et al. (2020) and Guan et al. (2020), we do not identify a dominance of dynamical convergence over advection. The magnitudes of moisture transport divergence in AR3 are ~~also much~~ lower. Nonetheless, we remind that Norris et al. (2020) and Guan et al. (2020) consider even more intense mid-latitude ~~AR~~ ARs near its centre. While AR3 is exceptionally strong for arctic conditions (Fig. 3), it is rather moderate for mid-latitude scales (Ralph et al., 2019).

Three synthetic sondes ~~in~~ per each frontal sector leg (located as for AR1 in Fig. 6) generally reproduce the divergence characteristics of the continuous reference ~~within~~ for each frontal sector (Fig. 13). The highest deviations occur for the cold sector, arising from mid-level moisture advection and low-level mass convergence overestimation. We note that slight cross-sectoral displacements of the sonde positions deviate the divergence characteristics, but they all maintain the ~~principle vertical characteristics~~ principal vertical features for each component and sector ~~(~~that is shown in Fig. 13~~)~~. When we contextualise our sonde results

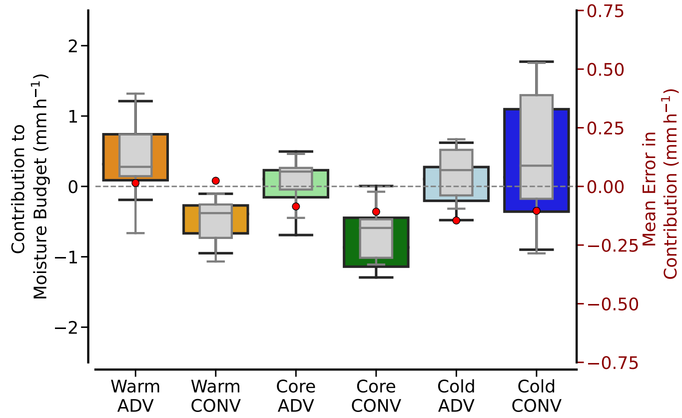

Figure 14. Box plot of moisture transport divergence contributions to daily moisture budget for all nine ARs. Values specify both components (ADV, $CONV$) for all frontal AR sectors (colour-coded). They compare the continuous AR representation (coloured box-whiskers) with the sonde-based values (grey). The boxes refer to the quartiles, and horizontal lines inside specify the respective mean.

with the mid-latitude based airborne study by Norris et al. (2020) using real dropsondes, we ~~recognize~~ recognise the strength of real sondes with a high vertical resolution. They provide much greater vertical variability. Thus, ~~it is likely that the quite low divergence displayed~~ the rather low divergence in Fig. 13 ~~does not only result from less~~ is probably not only the result of true lower divergence that prevails in arctic ~~ARs~~ ARs compared to mid-latitude ~~ARs, but may also be a consequence of~~ ARs. It can also result from the coarser vertical resolution~~averaging out larger values. Nevertheless, given the before mentioned contrasts of AR3 to mid-latitude AR moisture transport divergence, we should involve our other AR events in order to pinpoint robust~~, leading to spatial aliasing in narrow mass convergent low levels.

To pinpoint the commonalities and differences of the moisture transport divergence characteristics compared to mid-latitude ARs, and to what extent the airborne sondes can reproduce them (~~Q3-Q4).To compare moisture transport divergence for~~ Q3, Q4), we summarise all our arctic cases~~with statistics of mid-latitude ARs, we~~. We derive the vertical integral ∇IVT (Eq. 5) ~~. This quantifies~~ and quantify the contribution of moisture transport divergence to the moisture budget (Eq. 2) ~~. For our ARs, we summarise the daily contribution of~~ ~~∇IVT~~ in mm ~~d~~h^{-1}~~(~~. According to Fig. 14~~). Accordingly~~, the warm pre-frontal sector overall supplies moisture via advection that overcompensates weak mass divergence. In contrast, the core and post-frontal cold sector advection have ~~a~~ an inter-case variability in the advection of either dry or moist airmasses. In the post-frontal sector, both types of advection coexist. An overall large mass convergence in the post-frontal sector balances or even superimposes the advection. ~~The post-frontal sector marks the highest inter-event variability.~~ Surprisingly, the mass divergence in the core shows a robust negative contribution ~~for~~ to the moisture budget (Fig. 14).

~~For the arctic AR frontal sectors, the~~ The overall pre-frontal moisture advection in Fig. 14 is aligned with the profiles of AR3 (Fig. 13). Pre-frontal moisture advection primarily occurs in the mid-levels. The mass divergence in the core is surprising as most arctic ARs contain LLJs (Fig. 2) which are associated with high mass convergence in mid-latitude AR. However, the low-level mass convergence below 800 hPa, found in many of our AR cases like AR3 (Fig. 13), is often superimposed by mid-and upper-level mass divergence above the LLJ (e.g. Fig. 13), as the ARs spread out. The mass convergence in the post-frontal sector marks the highest inter-case variability. The high values of mass convergence, mostly from low-levels, as in Fig. 13, mainly arise from two cases (AR3, AR7). Here, we find changes in wind direction, as visible from the surface isobars in Fig. 1, inducing the confluence of moist air masses in the marine boundary layer. The sign of post-frontal advection is mainly determined by the intensity of dry air subsidence overrunning the western AR edge in mid-levels (see Fig. 2 and 13).

The range of budget contributions from -3 mm d^{-1} -1.5 to +31.5 mm d^{-1} mm h^{-1} of the arctic AR frontal sectors in Fig. 14 is quite small compared to smaller than mid-latitude AR magnitudes. For statistics Statistics of mid-latitude ARs , Guan et al. (2020) summarises in Guan et al. (2020) summarise budget contributions in the range -10 mm d^{-1} -2 to +152 mm d^{-1}. The mm h^{-1}. Especially, the moistening in the pre-frontal sector due to advection is similarly identified for arctic (Fig. 14) and mid-latitude ARs (Guan et al., 2020). In turn, the frontal characteristics of $CONV$ in arctic ARs contradict the understanding from Guan et al. (2020) who emphasized dominating mass convergence in and ahead of the AR embedded front for mid-latitude ARARs . Unlike the mid-latitudes, the upper-level dominating mass divergence in the core of arctic ARs is characterised by the divergence of mass. This is surprising as our arctic ARs, like mid-latitude AR, contain LLJs, see again Fig. 2, which are associated with high mass convergence. This mass convergence is also found in many of our AR cases, but often superimposed by mid-level mass divergence above the LLJ. For the pre-frontal sector, moistening due to moisture advection is similarly identified for arctic (Fig. 14) and mid-latitude ARs (Guan et al., 2020). In the post-frontal sector, both types of advection coexist, whereby the effectiveness of subsidence of dry air overrunning the AR in the mid-levels becomes crucial (see also Fig. 2). High values in post-frontal mass convergence mainly arise from two AR cases (AR3, AR7), where low-level changes in wind direction induce the convergence of air masses (see also Fig. 1lowers the triggering of precipitation by convection. Instead, major precipitation fields are often shifted towards higher reaching convergence west of the IVT maximum (not shown).

With six soundings per sector, the sondes reproduce the divergence characteristics (grey box-whiskers; Fig. 14), like the weak mass convergence that is ubiquitous for our arctic ARs. Overall, the sondes derive similar median values as the continuous AR representation and prove the fundamental observability of moisture transport divergence by discrete dropsondes. Six sondes per sector are basically capable to reproduce the general structure of moisture transport divergence across the AR and the vertically integrated contribution to the moisture budget. However, the percentiles between sondes and the continuous representation deviate. For individual events, sondes can misinterpret the magnitude of sector-specific divergence components considerably. Since this deviation is unbiased, though, the sonde mean errors remain below 0.1 mm h^{-1} (Fig. 14).

We emphasize that we cannot naively compare our frontal sector values with those of Guan et al. (2020)Nonetheless, the precedent comparison of our sector-based values of moisture transport divergence in arctic ARs to those in Guan et al. (2020) has to consider additional aspects. First, our arctic corridors along the sea ice edge are primarily attributed to the AR exit region, as the centre is located more southwards (see Fig. 3). For this exit region, we expect stronger divergence than convergence when the outflows of the ARs spread out. Guan et al. (2020) refer to the conditions across the AR centerscentres. Second, our frontal sectors are larger than those classified by single reanalysis pixel-based values used in Guan et al. (2020). Our sectors are, however, more comparable among the AR events as they are AR relative relative to AR strength and restrict to our defined

~~AR edges~~boundaries of the AR. Note that the post-frontal sector in Guan et al. (2020) is also more distant and exclusive from the actual AR, where we would already consider dissimilar flow patterns, such as southerly flow backside of the cyclone ~~in~~ (AR7~~. In~~ ; Fig. 1). Furthermore, Norris et al. (2020) highlight in their airborne case study ~~, Norris et al. (2020) highlight that much~~ that even higher values of moisture transport divergence occur at smaller scales than the reanalysis resolution used in Guan et al. (2020). Hence, we ~~postulate~~ assume that the sector-based values of moisture transport divergence ~~in~~ (Fig. 14) will also increase for smaller AR domains.

~~Box plot of moisture transport divergence contributions to daily moisture budget for all nine ARs. Values specify both components (ADV, $CONV$) for all frontal AR sectors (colour-coded). They compare the continuous AR representation (coloured box-whiskers) with the sonde-based values (grey). The boxes refer to the quartiles and horizontal lines inside specify the respective mean. Applying three soundings per cross-section sector, the sondes replicate the cross-frontal divergence (grey box-whiskers in Fig. 14), i.e. the weak mass convergence being omnipresent for our arctic ARs. The sonde configurations derive similar median values as the continuous AR representation and give evidence of the principle observability of moisture transport divergence by discrete dropsondes. Six sondes per sector are basically capable to reproduce the general frontal structure of moisture transport divergence and its vertically integrated contribution to the moisture budget. However, the percentiles between sondes and the continuous representation deviate. For individual events, sondes can misinterpret the magnitude of sector-specific divergence components considerably. Since this deviation is unbiased though, the sonde mean errors remain below $0.5\,\mathrm{mm\,d^{-1}}$ (Fig. 14). Another aspect not touched on in our discussion so far is~~ Another point not yet addressed is the fact that we mimic all observations of moisture transport divergence in terms of flight duration. This is a major difference from Guan et al. (2020), who derived divergence components for individual reanalysis time steps. ~~The~~ Our airborne continuous realisation (Sect. ~~??~~2.3) is non-instantaneous. This realisation can cause considerable deterioration in our understanding of the AR corridors due to the temporal AR evolution meanwhile. This issue is also ~~adressed in the airborne~~ addressed in the study of Norris et al. (2020), where they correct for the AR displacement over the flight duration by a time-to-space adjustment. However, they were not able to account for local temporal changes. Since our flight ~~patterns~~ pattern cover larger AR corridors than in Norris et al. (2020), it is ~~worth-investigating~~ worth investigating to what extent the temporal AR evolution during flight may distort the airborne moisture transport divergence results.

5 ~~Deterioration~~ Distortion by non-instantaneous soundings

This section examines the extent to which the temporal AR evolution during flight affects the sonde-based representation of IVT divergence ~~. Up~~ (Q4). During the up to 3 hours ~~are needed~~ it takes to fly over AR corridors ~~and consecutively~~ to observe the in- and outflow (Sect. ~~??). Meanwhile, temporal AR evolution can distort the airborne~~ (2.3), ARs evolve, resulting in non-instantaneous ~~) representation~~ observation of IVT divergence~~in the AR. Therefore~~. To quantify the deviations due to non-instantaneous observations, we establish an instantaneous reference ~~consisting of~~ with the spatially collocated AR representation at the ~~flight-centered hour and quantify the error in observed moisture transport that evolves over the flight duration~~centred hour of the flights. For the spatially continuous ~~AR~~ representation, we contrast the cross-frontal ∇IVT in

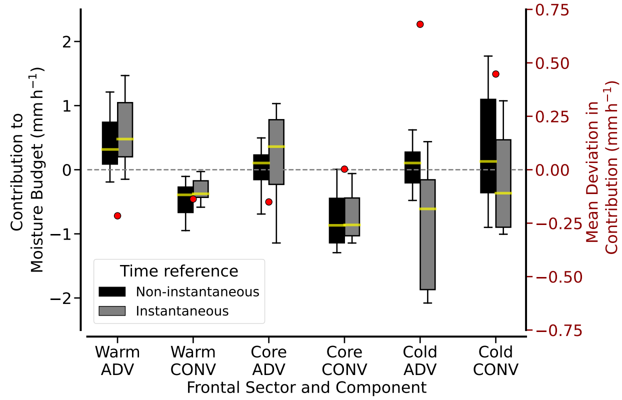

Figure 15. Comparison of divergence component contributions to daily moisture budget from spatially continuous AR representation, referring to either evolving flight values (non-instantaneous) or to the values for the ~~centered~~ centred hour (instantaneous). Values are given for each frontal sector. Black error bars are identical to the coloured boxes in Fig. 14. Grey values represent ~~centered~~ centred hour-based values. Red dots quantify the mean divergence deviations between both time references.

both temporal perspectives~~(~~, non-instantaneous and instantaneous~~)~~. For the sake of brevity, we call the latter the optimum airborne representation.

Summarising all ARs of Sect. 2.2, ~~Figure~~ Fig. 15 demonstrates that the frontal characteristics of ∇IVT are more or less reasonably reproduced by the non-instantaneous representation. However, we note that the mean deviations for the non-instantaneous ~~error in~~ divergence caused by the flight duration (red dots~~in~~; Fig. 15) ~~is~~ are much greater than ~~the error by discrete sondes (compare to~~ those by discrete sounding we showed in Fig. 14). In detail, the evolution of the ARs ~~deviates~~ changes the airborne estimates of prevailing moisture transport divergence by up to 25 % and even stronger on the backside of the AR. In the post-frontal sector, the mean ~~error exceeds 1.5 mm d^{-1}~~ deviation exceeds 0.5 mm h^{-1}, whereas sonde undersampling (Fig. 14) only induces mean ~~errors $\leq$ 0.5 mm d^{-1}~~ deviations $\leq$ 0.1 mm h^{-1}. The temporal evolution of the AR throughout the flight can thus strongly ~~deteriorate~~ change the divergence estimates for individual sectors. It is ADV in the post-frontal sector where we find the highest deviations compared to the instantaneous snapshot (Fig. 15). The deviations show up in the mean, median and standard deviation. ~~Not only does the instantaneous representationshow~~ The optimum airborne representation, that is instantaneous and spatially continuous, not only shows more robust post-frontal dry advection than the ~~airborne~~ non-instantaneous perspective, but there is also much greater case-to-case variability in its magnitude (~~-0.5 to -4~~0 to -2 ~~mm d^{-1}~~ mm h^{-1}) than seen ~~from the aircraft. When we consider~~ over the flight duration. Considering airborne (non-instantaneous) deviations for ~~individual~~ single ARs, we find cases with ~~errors~~ deviations in ADV that exceed more than ~~8~~2 ~~mm d^{-1} (not shown)~~ mm h^{-1}. In the pre-frontal sector and core, the median of $CONV$ is barely affected. ~~Although~~ $CONV$ has higher mean ~~errors~~ deviations in relative terms, but these have less influence on ~~the absolute deviation~~ absolute deviations of moisture transport divergence.

~~Referring to the ideal~~ For the optimum representation of ∇IVT in arctic AR cross-sections~~that is instantaneous and spatially continuous~~, the divergence characteristics in the ~~frontal sectors~~ AR sectors (Fig. 15) agree more with the mid-latitude statistics

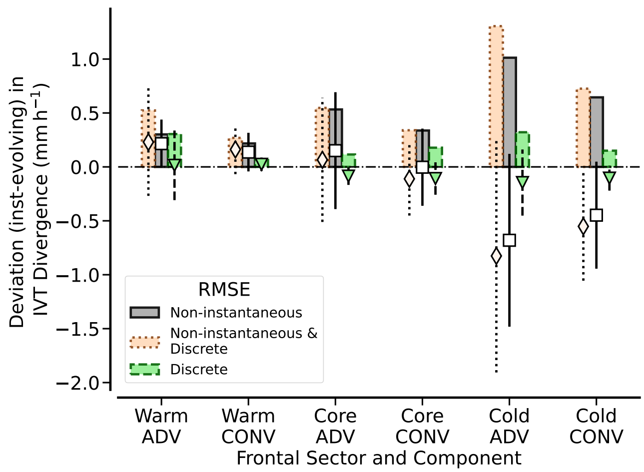

Figure 16. Total sonde ~~error~~ deviation (orange) and individual ~~errors~~ deviation by only discrete sondes (green) and by non-instantaneous sampling (grey) for daily IVT divergence in each frontal sector and divergence component (Eq. 5). For all ~~AR cross-sections~~ARs, positive bars indicate the root-mean-square error (RMSE), while error markers and lines depict mean ~~errors~~ deviations in combination with their standard deviations for ~~the~~ all ARs.

in Guan et al. (2020). In particular, we ~~also identify a frontal gradient~~ identify larger gradients in the divergence components across the front embedded in the AR, with overall moistening in the pre-frontal sector and drying in the post-frontal sector. In the arctic ARs, this is mainly driven by advection. Mass convergence being predominant in mid-latitude ~~ARs ishowever~~ ARs is, however, missing or is at least superimposed by mid-level mass divergence.

Having ~~just~~ confined ourselves to the spatially continuous representations of moisture transport divergence, we now contrast these with the sonde-based divergence resulting from the combination of non-instantaneous, and discrete spatial sampling (Sect. 4). To purely attribute the non-instantaneous effect on the divergence estimates at specific sonde locations, we hold the sonde positions fixed in both time perspectives. Thus, we do not relocate sondes once the sector-based IVT thresholds are exceeded at different locations in the instantaneous representation. Using the root-mean-square error (RMSE), ~~Figure~~ Fig. 16 compares the different spatial samplings (continuous and discrete) in both time perspectives~~with our reference, the instantaneous representation~~ , with the optimum airborne representation being our reference. ~~Accordingly, the subsampling errors~~ According to Fig. 16, the deviations caused by discrete subsampling are minor compared to ~~the errors induced by temporal~~ those induced by the temporal AR evolution and cannot compensate the latter, although they occasionally act in the opposite directions. The RMSEs for non-instantaneous sampling are ~~much~~ higher than the ones only induced by discrete sampling. Figure 16 underlines that the largest ~~errors~~ deviations occur in the cold post-frontal sector. While the RMSE for the combination of non-instantaneous and discrete subsampling in the warm pre-frontal sector and core is around or slightly below ~~1~~0.5 ~~$\mathrm{mm\,d^{-1}}$~~ $\mathrm{mm\,h^{-1}}$, the RMSE reaches up to ~~3~~1.5 ~~$\mathrm{mm\,d^{-1}}$~~ $\mathrm{mm\,h^{-1}}$ in the post-frontal sector. Non-instantaneous discrete sampling by sondes misrepresents the divergence components by more than 50 % of the actual values (compare with Fig. 15).

In turn, the RMSE resulting from the discrete subsampling alone only (green bars in Fig. 16) remains robustly below 1 mm d^{-1} mm h^{-1} throughout all frontal sectors.

The values of moisture advection are more sensitive to airborne sampling than mass divergence values. In contrast to discrete sampling, errors induced by instationarity in to ADV act in a more consistent direction (error bars in Fig. 16). In the cold sector, AR instationarity mainly leads to an underestimation of dry advection. These tendencies result from the oblique movement of the ARs which are not necessarily aligned with the moisture transport direction. In fact, our ARs move more or less to the northeast, while our flight pattern aims for cross-sections being orthogonal to the transport and are more zonally orientated. For the flight-centered flight centred hour (instantaneous reference), drier air masses are already more embedded in the post-frontal sector of the inflow cross-section leg, but less in the outflow leg. This changes the moisture gradient between both flight legs, increasing the overall dry advection. The winds exhibit less horizontal variability (Sect. 3.4). Temporal displacement thus varies $CONV$ less than ADV, so that $CONV$ remain less sensitive to non-instantaneous sampling.

We deduce that our flight pattern is subject to the strongest sonde-based misrepresentation in ∇IVT from advection in the cold post-frontal sector. Flight planning should involve weather forecasts to adapt the flight legs for AR evolution. Forecasts can estimate the mean propagation speed and direction of the AR corridor center centre so that in- and outflow legs can be shifted adequately. Similar to the error magnitudes, the inter-case variability in the divergence misrepresentation is much higher for advection (Fig. 16). The large inter-AR variability in the results highlights that more ARs should be considered in order to generalise the errors for to arctic ARs. This includes differentiating errors not only by the AR strength, but by their AR corridor type (entry, centre, exit). If flights are located in intense AR centres, we expect mass convergence to contribute more and errors due to sounding spacing to increase. The mass convergence may be more similar to the mid-latitude values in Guan et al. (2020). However, AR centers centres are rarely encountered near the sea ice in spring (Fig. 3). The occurrence of AR exit corridors over arctic sea ice is significantly higher. This underpins the usefulness of our error estimates for research flights in arctic ARs.

6 Conclusions and perspectives

This assessment study investigated the characteristics of the moisture transport divergence in arctic Atmospheric Rivers (ARs). We analysed the ARs conducted our analysis from an airborne perspective to assess the dropsonde-based observability of moisture transport divergence of arctic ARARs. We characterised airborne the uncertainties in sonde-based representation estimates of the AR moisture transport divergenceinside arctic ARs, focusing on two sonde-based limitations: subsampling by too large sounding spacing and the instationarity of the AR over the flight duration. For this, we followed a synthetic approach using reanalysis data as virtual truth. CARRA reanalysis data were interpolated on synthetic flight patterns that consist of two cross-sections covering frontal sectors over the entire AR transect. Single vertical profiles emulate dropsondes. We considered nine arctic AR events over the Atlantic pathway to the Arctic ocean Ocean in the vicinity of the sea-ice edge from last decade. The values of Integrated Water Vapour Transport (IVT) in the AR cores range from 300–600 kg m^{-1} s^{-1}, although the ARs are primarily examined north of their centercentre. We thus classify these ARs as overall strong for arctic conditions. Still, the bell shape of IVT across the AR varies strongly in between the AR cases. The ~~considered~~ cases cover a large variability and consist of various synoptic patterns (extended troughs, blocking situations, single cyclones) in which the ~~AR~~ ARs are embedded. This study delivers benchmarks of uncertainties in the airborne representation of sonde-based AR moisture transport divergence. We conclude the four pursued questions (Q1-Q4) as:

What is the maximum distance between sondes to determine the total moisture transport through AR corridors? (Q1)

– For the sonde-based determination of Total Integrated Water Vapour Transport ($TIVT$) in arctic AR cross-sections, sonde spacing below 100 km robustly keeps $TIVT$ errors below 10 % (Fig. 8). In strong ARs with IVT exceeding 500 kg m^{-1}s^{-1}, too coarse IVT representation at the AR core leads to $TIVT$ underestimation. Gaussian fits help to reproduce the cross-section IVT shape, but are sensitive to how sondes estimate the maximum IVT and its location. Thus, precedent flight planning should aim for a sonde release at the forecasted IVT maximum and place additional sondes symmetrically around. For arctic AR widths of 400–800 km, we suggest a minimum of seven soundings per cross-section (roughly ~~60 to 120~~60–120 km spacing) to derive $TIVT$ in both cross-section legs. The maximum IVT is more correlated to IVT variability than the AR width is. The planning of sonde releases should thus rely on the steepness of IVT along the cross-section. We highlight that the differences of $TIVT$ between the in- and outflow cross-sections are in a range of 2–15 % (Fig. 12). If we want to reliably estimate moisture transport divergence based on $TIVT$ from both cross-sections, the sonde-based uncertainty of $TIVT$ for a single flight leg must be considerably lower.

How correlated are moisture and winds in arctic ARs and do coherent patterns contribute significantly to IVT? (Q2)

– Moisture and wind in arctic ARs along the flight transects are only moderately correlated~~with~~, with a mean correlation coefficient of 0.5 at about 850 hPa height and less ~~below and above~~at other heights. At the same time, the standard deviation of both quantities is smaller than its mean, respectively. Moderate correlation and limited variability result in a small contribution of coherent patterns to IVT, which is smaller than 10 % of the moisture transport by the mean quantities. We draw the conclusion that collocated sampling of wind and moisture to assess the coherent transport is not of first priority. It is ~~worth noting~~ notable that the moisture variability dominates the wind variability over most of the profile between 850 and 500 hPa. Only close to the surface, the wind variability peaks at about 850 hPa and plays an essential role. ~~Thus~~When faced with a limited number of dropsondes, we prioritise supplementary airborne measurements of moisture to better represent arctic AR-IVT variability.

How can the divergence of moisture transport be characterised along cross-sections of arctic ARs? (Q3)

– By contrasting the in- and outflow $TIVT$ through both cross-sections of all ARs, we expect an overall divergence in moisture transport. Yet, the ARs show frontal specific characteristics in IVT divergence, which have to be separated into moisture advection (ADV) and mass convergence ($CONV$), see Sect. 4. The moisture advection on the arctic AR edges is most contributing to the moisture transport divergence. The pre-frontal AR sectors contribute to the moisture budget via moisture advection, while the post-frontal sectors generally show dry advection, but also occasional mass convergence. However, in contrast to mid-latitude ARs, mass convergence is much less dominant in the ~~Arctic~~ arctic

ARs. Although the mass convergence is generally dominant, especially below 850hPa, it is often superimposed by hPa, upper-level divergence often superimposes it. In turn, moisture advection is much more relevant and dominates at levels higher than 850 hPa. Across the front, the total contribution of IVT divergence to the moisture budget is up to +3 1 mm h^{-1} (pre-frontal moisture advection) to -3 mm d^{-1} 2 mm h^{-1} (post-frontal dry advection). This is less than half the magnitude compared to the mid-latitudes. slightly less than the magnitudes in mid-latitude ARs.

To what extent can non-instantaneous sondes reproduce IVT divergence in the light of AR evolution during flight? (Q4)

– Three sondes per frontal For reproducing IVT divergence, the undersampling by a limited number of sondes matters. We recommend a sequence of at least seven sondes per AR cross-section. Given the widths of arctic ARs, this corresponds to a maximum sonde spacing of 100 km. Symmetrically placed around the maximum IVT, three sondes per AR sector leg are capable to reproduce the frontal of reproducing the sector characteristics of moisture transport divergence components with similar magnitudes. The mean absolute error to the deviations to a continuous AR representation along the flight extends to around 0.5reach up to 0.1 mm d^{-1} mm h^{-1} (Fig. 14). Sonde-based estimates are most sensitive However, the deviations for moisture transport divergence by undersampling are minor compared to the deviations induced by the flight duration, that mostly range from 25–50 % of the actual divergence values (Fig. 16). Non-instantaneous sonde-based estimates deviate the most in the post-frontal cold sector, where we also detect steeper gradients in moisture and winds than in the pre-frontal sectors. There is, in turn, high inter-case spread with positive and negative deviations. Noteworthy is that the error for moisture transport divergence by undersampling becomes minor compared to the error induced by the flight duration. For the post-frontal cold sector, the temporal AR evolution during the flight is responsible Here, the AR displacement during flight, which is not necessarily along the moisture transport direction, as well as the intensity of dry intrusions on the backside of the AR is relevant for more than twice the deviations in ADV and $CONV$. The divergence errors can exceed , partly exceeding 50 % of the actual values. Unlike the undersamplingerrors, non-instantaneous sampling induces errors in a more consistent direction. Especially in the effects deteriorate the results more consistently. Advection estimates are overall most affected by the airborne sampling. In fact, the pre-frontal moisture advection and the post-frontal sector, the divergence is stronger for both, sector divergence (from ADV and $CONV$) are stronger than assumed by the sondes. Here the intensity and pace of dry intrusions on the backside of the AR front plays a fundamental rule in the distortion of airborne sonde-based moisture transport divergence estimates. We conclude that moisture advection on the arctic AR edges is most contributing to the moisture transport divergence and in the post-frontal most sensitive to the airborne strategy as the ARs do not necessarily displace along the moisture transport direction. Although mass convergence is much less predominant than in mid-latitude ARs, directional convergence becomes relevantin the post-frontal sector, but sondes. Although post-frontal mass confluence is relevant, it is overestimated by sondes during flight.

We The synthetic sondes confirm the observability of moisture transport divergence in arctic AR corridors by releasing sondes in such dedicated flight patterns . A maximum sonde spacing of 100 km within the AR cross-section can in principle characterise the divergence between both cross-sections with the given uncertainties of $\leq 10\,\%$. For the flight duration, we

~~obtain the moisture transport divergence specified for frontal sectors with an uncertainty in the range of 25–50 %. We deduce that sonde undersampling matters and recommend a sequence of at least seven sondes per section given the widths of arctic ARs. However, notwithstanding~~ dropsondes in zigzag flight patterns in the future. Notwithstanding that we could release ~~a higher number of~~ more sondes, it is the temporal evolution of the AR over the flight duration that leads to higher deviations in the divergence components rather than sonde undersampling. ~~The~~ Therefore, the dedicated planning of such sonde-based purposes should not only include the ~~positioning of the sondes~~sonde positioning, but also the minimisation of the flight duration. The placement of cross-section legs and their spacing should carefully consider the AR displacement during flight. Shorter distances between the cross-sections not only reduce the flight duration, but also the area enclosed by sondes. Given the ~~frontal-sector~~ widths of the arctic ARs sectors, both cross-sections should be no more than 200 km apart. For several of our cases, the meridional separation is higher, and we have to expect considerable subgrid scale variability. ~~Collocated~~ The optimal and still feasible strategy represents collocated flights by two aircraft, with both cross-sections being not far apart and sampled simultaneously~~, is the optimal and still feasible strategy. When faced with a limited number of dropsondes, supplementary~~ . Supplementary measurements of moisture should be prioritised ~~, as moisture is the more variable quantity and moisture advection mostly dominates the moisture transport divergence in the arctic AR corridors~~due to its higher variability, and its advection dominating ∇IVT.

Additional limitations of our study need to be discussed. ~~As~~ All our conclusions, especially the described AR characteristics, are drawn from simulations and should be verified with observations, as the extent to which the simulations reproduce the small-scale variability is uncertain. Furthermore, as our results are mainly based on corridors in the AR exit region, we strongly recommend extending our uncertainty assessment to other AR regions and expect the role of winds and mass convergence to increase in strong AR ~~centers~~centres. This becomes an even more important issue with respect to the tendency of arctic ARs to shift more northward and intensify under climate change (O'Brien et al., 2022). Furthermore, as we include a large variability of synoptic AR patterns but a small sample, we propose follow-up statistics with a larger number of AR events. The statistics can improve our understanding of the moisture transport divergence ~~patterns~~ pattern in arctic ARs and attribute it to the dynamic and thermodynamic atmospheric conditions. ~~Here~~For this purpose, CARRA represents a very suitable reanalysis framework~~for this purpose in follow-up studies~~. Again, we encourage the use of the higher vertical resolution of the model levels rather than our chosen pressure levels, although they were sufficient for initial estimates. For real sondes, we emphasise the added value of their high vertical resolution. Sondes provide more accurate information on the vertical composition of ADV and $CONV$. The sonde-based approach is limited to regression-based divergence~~where we consider only rather~~ , where we only consider large areas and open meridional boundaries. Even with continuous lateral sampling, the meridional gradients are only coarsely sampled.

Therefore, a follow-up study should investigate how the arctic AR moisture transport divergence acts inside the flight corridor at grid-cell scales. This will allow two additional ~~research~~ topics to be addressed: First, the internal variability between both cross-sections can be derived more precisely to improve the flight ~~pattern, second~~patterns, second, the actual scales at which the moisture transport divergence varies significantly can be evaluated. This may ~~also~~ increase the divergence magnitudes, similarly to Norris et al. (2020) who found larger values of the divergence components. They considered smaller airborne AR corridors than the ERA-Interim pixels referred to in Guan et al. (2020).

Despite the aforementioned above limitations, the orders of magnitudes magnitude for IVT variability and divergence that we provide are representative for arctic ARs and quantify benchmarks in for the sonde-based derivation. Consistently mimicking the soundings is a fundamental step towards the understanding of the uncertainties when such airborne tactics are actually carried outEmulated soundings assess possible airborne misrepresentation in moisture transport divergence and will improve the interpretation of future real soundings aiming for the airborne closure of the moisture budget in ARs. The benchmarks are not only useful for improving flight strategies, but also indicate deviations in corresponding model-observation comparisons. Only by illuminating the constraints on the AR representation from both models and observations, we establish a framework from which With the quantified uncertainties in the sonde-based AR representation of IVT divergence, future airborne observations can support better assist modellers in terms of the resolution and complexity required for parameterisation of to represent predominant moisture transformation processes caused by IVT divergence in arctic ARs.

Code and data availability. The code created by HD analysing the downloaded reanalyses and creates the figures can be accessed via github and is made available under: https://github.com/hdorff94/Synthetic_Airborne_Arctic_ARs. The reanalysis data from CARRA (Schyberg et al., 2021) and ERA5 (Hersbach et al., 2018) were accessed from the Copernicus Climate Change Service(C3S) Climate Data Store (CDS). The AR catalogue (Guan, 2022) used to pre-identify AR events of interest is provided by Bin Guan via https://ucla.box.com/ARcatalog.

Author contributions. HD, FA and HK were main initiators for the work in the scope of this manuscript. FA, HK and VS helped to conceptualise the manuscript. HD conducted the analysis presented and drafted the manuscript under scientific supervision of FA, HK and VS. All authors contributed to revising the manuscript.

Competing interests. The authors declare that they have no conflict of interest.

Acknowledgements. This study was supported by the Deutsche Forschungsgemeinschaft (DFG; German Research Foundation) under the HALO SPP 1294. We thank the two anonymous reviewers, for providing us with helpful comments that improved the quality of the paper, and the associate editor Geraint Vaughan. We explicitly acknowledge the Copernicus Climate Change Service (C3S) Climate Data Store (CDS) for providing access to CARRA and ERA5 data. We thank Bin Guan for making the AR catalogue publically available via https://ucla.box.com/ARcatalog. Furthermore, we want to thank Melanie Lauer and Geet George for various helpful discussions. Henning Dorff is thankful to Jochem Marotzke and Dallas Murphy for providing fruitful comments on the writing style and structure of the manuscript. Thanks also go towards Norbert Noreiks for delivering sketches of the research aircraft.

References

Bengtsson, L., Andrae, U., Aspelien, T., Batrak, Y., Calvo, J., de Rooy, W., Gleeson, E., Hansen-Sass, B., Homleid, M., Hortal, M., Ivarsson, K.-I., Lenderink, G., Niemelä, S., Nielsen, K. P., Onvlee, J., Rontu, L., Samuelsson, P., Muñoz, D. S., Subias, A., Tijm, S., Toll, V., Yang, X., and Køltzow, M. Ø.: The HARMONIE–AROME Model Configuration in the ALADIN–HIRLAM NWP System, Monthly Weather Review, 145, 1919–1935, https://doi.org/10.1175/mwr-d-16-0417.1, 2017.

Bony, S. and Stevens, B.: Measuring Area-Averaged Vertical Motions with Dropsondes, Journal of the Atmospheric Sciences, 76, 767–783, https://doi.org/10.1175/jas-d-18-0141.1, 2019.

Cobb, A., Michaelis, A., Iacobellis, S., Ralph, F. M., and Monache, L. D.: Atmospheric River Sectors: Definition and Characteristics Observed Using Dropsondes from 2014–20 CalWater and AR Recon, Monthly Weather Review, 149, 623–644, https://doi.org/10.1175/mwr-d-20-0177.1, 2021a.

Cobb, A., Monache, L. D., Cannon, F., and Ralph, F. M.: Representation of Dropsonde-Observed Atmospheric River Conditions in Reanalyses, Geophysical Research Letters, 48, https://doi.org/10.1029/2021gl093357, 2021b.

Cobb, A., Ralph, F. M., Tallapragada, V., Wilson, A. M., Davis, C. A., Monache, L. D., Doyle, J. D., Pappenberger, F., Reynolds, C. A., Subramanian, A., Black, P. G., Cannon, F., Castellano, C., Cordeira, J. M., Haase, J. S., Hecht, C., Kawzenuk, B., Lavers, D. A., Murphy, M. J., Parrish, J., Rickert, R., Rutz, J. J., Torn, R., Wu, X., and Zheng, M.: Atmospheric River Reconnaissance 2021: A Review, Weather and Forecasting, https://doi.org/10.1175/waf-d-21-0164.1, 2022.

Cordeira, J. M., Ralph, F. M., and Moore, B. J.: The Development and Evolution of Two Atmospheric Rivers in Proximity to Western North Pacific Tropical Cyclones in October 2010, Monthly Weather Review, 141, 4234–4255, https://doi.org/10.1175/mwr-d-13-00019.1, 2013.

Dacre, H. F., Martínez-Alvarado, O., and Mbengue, C. O.: Linking Atmospheric Rivers and Warm Conveyor Belt Airflows, Journal of Hydrometeorology, 20, 1183–1196, https://doi.org/10.1175/jhm-d-18-0175.1, 2019.

Dee, D. P., Uppala, S. M., Simmons, A. J., Berrisford, P., Poli, P., Kobayashi, S., Andrae, U., Balmaseda, M. A., Balsamo, G., Bauer, P., Bechtold, P., Beljaars, A. C. M., van de Berg, L., Bidlot, J., Bormann, N., Delsol, C., Dragani, R., Fuentes, M., Geer, A. J., Haimberger, L., Healy, S. B., Hersbach, H., Hólm, E. V., Isaksen, L., Kållberg, P., Köhler, M., Matricardi, M., McNally, A. P., Monge-Sanz, B. M., Morcrette, J., Park, B., Peubey, C., de Rosnay, P., Tavolato, C., Thépaut, J., and Vitart, F.: The ERA-Interim reanalysis: configuration and performance of the data assimilation system, Quarterly Journal of the Royal Meteorological Society, 137, 553–597, https://doi.org/10.1002/qj.828, 2011.

Demirdjian, R., Norris, J. R., Martin, A., and Ralph, F. M.: Dropsonde Observations of the Ageostrophy within the Pre-Cold-Frontal Low-Level Jet Associated with Atmospheric Rivers, Monthly Weather Review, 148, 1389–1406, https://doi.org/10.1175/mwr-d-19-0248.1, 2020.

Dufour, A., Zolina, O., and Gulev, S. K.: Atmospheric Moisture Transport to the Arctic: Assessment of Reanalyses and Analysis of Transport Components, Journal of Climate, 29, 5061–5081, https://doi.org/10.1175/jcli-d-15-0559.1, 2016.

Fearon, M. G., Doyle, J. D., Ryglicki, D. R., Finocchio, P. M., and Sprenger, M.: The Role of Cyclones in Moisture Transport into the Arctic, Geophysical Research Letters, 48, https://doi.org/10.1029/2020gl090353, 2021.

George, G., Stevens, B., Bony, S., Pincus, R., Fairall, C., Schulz, H., Kölling, T., Kalen, Q. T., Klingebiel, M., Konow, H., Lundry, A., Prange, M., and Radtke, J.: JOANNE: Joint dropsonde Observations of the Atmosphere in tropical North atlaNtic meso-scale Environments, Earth System Science Data, 13, 5253–5272, https://doi.org/10.5194/essd-13-5253-2021, 2021.

Graham, R. M., Cohen, L., Ritzhaupt, N., Segger, B., Graversen, R. G., Rinke, A., Walden, V. P., Granskog, M. A., and Hudson, S. R.: Evaluation of Six Atmospheric Reanalyses over Arctic Sea Ice from Winter to Early Summer, Journal of Climate, 32, 4121–4143, https://doi.org/10.1175/jcli-d-18-0643.1, 2019.

Guan, B.: Tracking Atmospheric Rivers Globally as Elongated Targets (tARget), Version 3 [Dataset], https://doi.org/10.25346/S6/YO15ON, 2022.

Guan, B. and Waliser, D. E.: Detection of atmospheric rivers: Evaluation and application of an algorithm for global studies, Journal of Geophysical Research: Atmospheres, 120, 12 514–12 535, https://doi.org/10.1002/2015jd024257, 2015.

Guan, B. and Waliser, D. E.: Atmospheric rivers in 20 year weather and climate simulations: A multimodel, global evaluation, Journal of Geophysical Research: Atmospheres, 122, 5556–5581, https://doi.org/10.1002/2016jd026174, 2017.

Guan, B. and Waliser, D. E.: Tracking Atmospheric Rivers Globally: Spatial Distributions and Temporal Evolution of Life Cycle Characteristics, Journal of Geophysical Research: Atmospheres, 124, 12 523–12 552, https://doi.org/10.1029/2019jd031205, 2019.

Guan, B., Waliser, D. E., and Ralph, F. M.: An Intercomparison between Reanalysis and Dropsonde Observations of the Total Water Vapor Transport in Individual Atmospheric Rivers, Journal of Hydrometeorology, 19, 321–337, https://doi.org/10.1175/jhm-d-17-0114.1, 2018.

Guan, B., Waliser, D. E., and Ralph, F. M.: A multimodel evaluation of the water vapor budget in atmospheric rivers, Annals of the New York Academy of Sciences, 1472, 139–154, https://doi.org/10.1111/nyas.14368, 2020.

Guan, B., Waliser, D. E., and Ralph, F. M.: Global Application of the Atmospheric River Scale, Journal of Geophysical Research: Atmospheres, 128, https://doi.org/10.1029/2022jd037180, 2023.

Hersbach, H., Bell, B., Berrisford, P., Biavati, G., Horanyi, A., Sabater, J. M., Nicolas, J., Peubey, C., Radu, R., Rozum, I., Schepers, D., Simmons, A., Soci, C., Dee, D., and Thepaut, J.-N.: ERA5 hourly data on pressure levels from 1940 to present, Copernicus Climate Change Service (C3S) Climate Data Store (CDS) [data set] (accessed 22-Apr-2022), https://doi.org/10.24381/cds.bd0915c6, 2018.

Hersbach, H., Bell, B., Berrisford, P., Hirahara, S., Nicolas, J., Peubey, C., Radu, R., Schepers, D., Simmons, A., Soci, C., Abdalla, S., Abellan, X., Balsamo, G., Bechtold, P., Biavati, G., Bidlot, J., Bonavita, M., Chiara, G., Dahlgren, P., Dee, D., Diamantakis, M., Dragani, R., Flemming, J., Forbes, R., Fuentes, M., Geer, A., Haimberger, L., Healy, S., Hogan, R. J., Keeley, S., Laloyaux, P., Lopez, P., Lupu, C., Radnoti, G., Rosnay, P., Rozum, I., Vamborg, F., and Villaume, S.: The ERA5 global reanalysis, Quarterly Journal of the Royal Meteorological Society, 146, 1999–2049, https://doi.org/10.1002/qj.3803, 2020.

Kirbus, B., Tiedeck, S., Camplani, A., Chylik, J., Crewell, S., Dahlke, S., Ebell, K., Gorodetskaya, I., Griesche, H., Handorf, D., Höschel, I., Lauer, M., Neggers, R., Rückert, J., Shupe, M. D., Spreen, G., Walbröl, A., Wendisch, M., and Rinke, A.: Surface impacts and associated mechanisms of a moisture intrusion into the Arctic observed in mid-April 2020 during MOSAiC, Frontiers in Earth Science, 11, https://doi.org/10.3389/feart.2023.1147848, 2023.

Køltzow, M., Schyberg, H., Støylen, E., and Yang, X.: Value of the Copernicus Arctic Regional Reanalysis (CARRA) in representing near-surface temperature and wind speed in the north-east European Arctic, Polar Research, 41, https://doi.org/10.33265/polar.v41.8002, 2022.

Komatsu, K. K., Alexeev, V. A., Repina, I. A., and Tachibana, Y.: Poleward upgliding Siberian atmospheric rivers over sea ice heat up Arctic upper air, Scientific Reports, 8, https://doi.org/10.1038/s41598-018-21159-6, 2018.

Konow, H., Jacob, M., Ament, F., Crewell, S., Ewald, F., Hagen, M., Hirsch, L., Jansen, F., Mech, M., and Stevens, B.: A unified data set of airborne cloud remote sensing using the HALO Microwave Package (HAMP), Earth System Science Data, 11, 921–934, https://doi.org/10.5194/essd-11-921-2019, 2019.

Konow, H., Ewald, F., George, G., Jacob, M., Klingebiel, M., Kölling, T., Luebke, A. E., Mieslinger, T., Pörtge, V., Radtke, J., Schäfer, M., Schulz, H., Vogel, R., Wirth, M., Bony, S., Crewell, S., Ehrlich, A., Forster, L., Giez, A., Gödde, F., Groß, S., Gutleben, M., Hagen, M., Hirsch, L., Jansen, F., Lang, T., Mayer, B., Mech, M., Prange, M., Schnitt, S., Vial, J., Walbröl, A., Wendisch, M., Wolf, K., Zinner, T., Zöger, M., Ament, F., and Stevens, B.: EUREC4A's HALO, Earth System Science Data, 13, 5545–5563, https://doi.org/10.5194/essd-13-5545-2021, 2021.

Lauer, M., Mech, M., and Guan, B.: Global Atmospheric Rivers catalog for ERA5 reanalysis, https://doi.org/10.1594/PANGAEA.957161, 2023a.

Lauer, M., Rinke, A., Gorodetskaya, I., Sprenger, M., Mech, M., and Crewell, S.: Influence of atmospheric rivers and associated weather systems on precipitation in the Arctic, Atmospheric Chemistry and Physics, 23, 8705–8726, https://doi.org/10.5194/acp-23-8705-2023, 2023b.

Lenschow, D. H., Savic-Jovcic, V., and Stevens, B.: Divergence and Vorticity from Aircraft Air Motion Measurements, Journal of Atmospheric and Oceanic Technology, 24, 2062–2072, https://doi.org/10.1175/2007jtecha940.1, 2007.

Mattingly, K. S., Mote, T. L., and Fettweis, X.: Atmospheric River Impacts on Greenland Ice Sheet Surface Mass Balance, JGR Atmospheres, 123, 8538–8560, https://doi.org/10.1029/2018jd028714, 2018.

Mech, M., Orlandi, E., Crewell, S., Ament, F., Hirsch, L., Hagen, M., Peters, G., and Stevens, B.: HAMP – the microwave package on the High Altitude and LOng range research aircraft (HALO), Atmospheric Measurement Techniques, 7, 4539–4553, https://doi.org/10.5194/amt-7-4539-2014, 2014.

Nash, D., Waliser, D., Guan, B., Ye, H., and Ralph, F. M.: The Role of Atmospheric Rivers in Extratropical and Polar Hydroclimate, Journal of Geophysical Research: Atmospheres, 123, 6804–6821, https://doi.org/10.1029/2017jd028130, 2018.

Neff, W.: Atmospheric rivers melt Greenland, 8, 857–858, https://doi.org/10.1038/s41558-018-0297-4, 2018.

Neff, W., Compo, G. P., Ralph, F. M., and Shupe, M. D.: Continental heat anomalies and the extreme melting of the Greenland ice surface in 2012 and 1889, Journal of Geophysical Research: Atmospheres, 119, 6520–6536, https://doi.org/10.1002/2014jd021470, 2014.

Neiman, P. J., Wick, G. A., Moore, B. J., Ralph, F. M., Spackman, J. R., and Ward, B.: An Airborne Study of an Atmospheric River over the Subtropical Pacific during WISPAR: Dropsonde Budget-Box Diagnostics and Precipitation Impacts in Hawaii, Monthly Weather Review, 142, 3199–3223, https://doi.org/10.1175/mwr-d-13-00383.1, 2014.

Norris, J. R., Ralph, F. M., Demirdjian, R., Cannon, F., Blomquist, B., Fairall, C. W., Spackman, J. R., Tanelli, S., and Waliser, D. E.: The Observed Water Vapor Budget in an Atmospheric River over the Northeast Pacific, Journal of Hydrometeorology, 21, 2655–2673, https://doi.org/10.1175/jhm-d-20-0048.1, 2020.

Nygård, T., Naakka, T., and Vihma, T.: Horizontal Moisture Transport Dominates the Regional Moistening Patterns in the Arctic, Journal of Climate, 33, 6793–6807, https://doi.org/10.1175/jcli-d-19-0891.1, 2020.

O'Brien, T. A., Wehner, M. F., Payne, A. E., Shields, C. A., Rutz, J. J., Leung, L.-R., Ralph, F. M., Collow, A., Gorodetskaya, I., Guan, B., Lora, J. M., McClenny, E., Nardi, K. M., Ramos, A. M., Tomé, R., Sarangi, C., Shearer, E. J., Ullrich, P. A., Zarzycki, C., Loring, B., Huang, H., Inda-Díaz, H. A., Rhoades, A. M., and Zhou, Y.: Increases in Future AR Count and Size: Overview of the ARTMIP Tier 2 CMIP5/6 Experiment, Journal of Geophysical Research: Atmospheres, 127, https://doi.org/10.1029/2021jd036013, 2022.

Papritz, L. and Dunn-Sigouin, E.: What Configuration of the Atmospheric Circulation Drives Extreme Net and Total Moisture Transport Into the Arctic, Geophysical Research Letters, 47, https://doi.org/10.1029/2020gl089769, 2020.

Papritz, L., Aemisegger, F., and Wernli, H.: Sources and Transport Pathways of Precipitating Waters in Cold-Season Deep North Atlantic Cyclones, Journal of the Atmospheric Sciences, 78, 3349–3368, https://doi.org/10.1175/jas-d-21-0105.1, 2021.

Ralph, F. M., Neiman, P. J., and Wick, G. A.: Satellite and CALJET Aircraft Observations of Atmospheric Rivers over the Eastern North Pacific Ocean during the Winter of 1997/98, Monthly Weather Review, 132, 1721–1745, https://doi.org/10.1175/1520-0493(2004)132<1721:sacaoo>2.0.co;2, 2004.

Ralph, F. M., Neiman, P. J., and Rotunno, R.: Dropsonde Observations in Low-Level Jets over the Northeastern Pacific Ocean from CALJET-1998 and PACJET-2001: Mean Vertical-Profile and Atmospheric-River Characteristics, 133, 889–910, https://doi.org/10.1175/mwr2896.1, 2005.

Ralph, F. M., Iacobellis, S. F., Neiman, P. J., Cordeira, J. M., Spackman, J. R., Waliser, D. E., Wick, G. A., White, A. B., and Fairall, C.: Dropsonde Observations of Total Integrated Water Vapor Transport within North Pacific Atmospheric Rivers, Journal of Hydrometeorology, 18, 2577–2596, https://doi.org/10.1175/jhm-d-17-0036.1, 2017.

Ralph, F. M., Rutz, J. J., Cordeira, J. M., Dettinger, M., Anderson, M., Reynolds, D., Schick, L. J., and Smallcomb, C.: A Scale to Characterize the Strength and Impacts of Atmospheric Rivers, Bulletin of the American Meteorological Society, 100, 269–289, https://doi.org/10.1175/bams-d-18-0023.1, 2019.

Rostosky, P. and Spreen, G.: Relevance of warm air intrusions for Arctic satellite sea ice concentration time series, The Cryosphere, 17, 3867–3881, https://doi.org/10.5194/tc-17-3867-2023, 2023.

Schyberg, H., Yang, X., Koltzow, M., Amstrup, B., Bakketun, A., Bazile, E., Bojarova, J., Box, J. E., Dahlgren, P., Hagelin, S., Homleid, M., Horanyi, A., Hoyer, J., Johansson, A., Killie, M., Koernich, H., Moigne, P. L., Lindskog, M., Manninen, T., Englyst, P. N., Nielsen, K., Olsson, E., Palmason, B., Aros, C. P., Randriamampianina, R., Samuelsson, P., Stappers, R., Stoylen, E., Thorsteinsson, S., Valkonen, T., and Wang, Z.: Arctic regional reanalysis on pressure levels from 1991 to present, Copernicus Climate Change Service (C3S) Climate Data Store(CDS) (accessed on 16-Jun-2022), https://doi.org/10.24381/CDS.E3C841AD, 2021.

Seager, R. and Henderson, N.: Diagnostic Computation of Moisture Budgets in the ERA-Interim Reanalysis with Reference to Analysis of CMIP-Archived Atmospheric Model Data, Journal of Climate, 26, 7876–7901, https://doi.org/10.1175/jcli-d-13-00018.1, 2013.

Shupe, M. D., Rex, M., Blomquist, B., Persson, P. O. G., Schmale, J., Uttal, T., Althausen, D., Angot, H., Archer, S., Bariteau, L., Beck, I., Bilberry, J., Bucci, S., Buck, C., Boyer, M., Brasseur, Z., Brooks, I. M., Calmer, R., Cassano, J., Castro, V., Chu, D., Costa, D., Cox, C. J., Creamean, J., Crewell, S., Dahlke, S., Damm, E., de Boer, G., Deckelmann, H., Dethloff, K., Dütsch, M., Ebell, K., Ehrlich, A., Ellis, J., Engelmann, R., Fong, A. A., Frey, M. M., Gallagher, M. R., Ganzeveld, L., Gradinger, R., Graeser, J., Greenamyer, V., Griesche, H., Griffiths, S., Hamilton, J., Heinemann, G., Helmig, D., Herber, A., Heuzé, C., Hofer, J., Houchens, T., Howard, D., Inoue, J., Jacobi, H.-W., Jaiser, R., Jokinen, T., Jourdan, O., Jozef, G., King, W., Kirchgaessner, A., Klingebiel, M., Krassovski, M., Krumpen, T., Lampert, A., Landing, W., Laurila, T., Lawrence, D., Lonardi, M., Loose, B., Lüpkes, C., Maahn, M., Macke, A., Maslowski, W., Marsay, C., Maturilli, M., Mech, M., Morris, S., Moser, M., Nicolaus, M., Ortega, P., Osborn, J., Pätzold, F., Perovich, D. K., Petäjä, T., Pilz, C., Pirazzini, R., Posman, K., Powers, H., Pratt, K. A., Preußer, A., Quéléver, L., Radenz, M., Rabe, B., Rinke, A., Sachs, T., Schulz, A., Siebert, H., Silva, T., Solomon, A., Sommerfeld, A., Spreen, G., Stephens, M., Stohl, A., Svensson, G., Uin, J., Viegas, J., Voigt, C., von der Gathen, P., Wehner, B., Welker, J. M., Wendisch, M., Werner, M., Xie, Z., and Yue, F.: Overview of the MOSAiC expedition: Atmosphere, Elementa: Science of the Anthropocene, 10, https://doi.org/10.1525/elementa.2021.00060, 2022.

Skamarock, W. C., Park, S.-H., Klemp, J. B., and Snyder, C.: Atmospheric Kinetic Energy Spectra from Global High-Resolution Nonhydrostatic Simulations, Journal of the Atmospheric Sciences, 71, 4369–4381, https://doi.org/10.1175/jas-d-14-0114.1, 2014.

Stevens, B., Ament, F., Bony, S., Crewell, S., Ewald, F., Gross, S., Hansen, A., Hirsch, L., Jacob, M., Kölling, T., Konow, H., Mayer, B., Wendisch, M., Wirth, M., Wolf, K., Bakan, S., Bauer-Pfundstein, M., Brueck, M., Delanoë, J., Ehrlich, A., Farrell, D., Forde, M., Gödde, F., Grob, H., Hagen, M., Jäkel, E., Jansen, F., Klepp, C., Klingebiel, M., Mech, M., Peters, G., Rapp, M., Wing, A. A., and Zinner, T.: A High-Altitude Long-Range Aircraft Configured as a Cloud Observatory: The NARVAL Expeditions, Bulletin of the American Meteorological Society, 100, 1061–1077, https://doi.org/10.1175/bams-d-18-0198.1, 2019.

Terpstra, A., Gorodetskaya, I. V., and Sodemann, H.: Linking Sub-Tropical Evaporation and Extreme Precipitation Over East Antarctica: An Atmospheric River Case Study, Journal of Geophysical Research: Atmospheres, 126, https://doi.org/10.1029/2020jd033617, 2021.

Vázquez, M., Algarra, I., Eiras-Barca, J., Ramos, A. M., Nieto, R., and Gimeno, L.: Atmospheric Rivers over the Arctic: Lagrangian Characterisation of Their Moisture Sources, Water, 11, 41, https://doi.org/10.3390/w11010041, 2018.

Viceto, C., Gorodetskaya, I. V., Rinke, A., Maturilli, M., Rocha, A., and Crewell, S.: Atmospheric rivers and associated precipitation patterns during the ACLOUD and PASCAL campaigns near Svalbard (May–June 2017): case studies using observations, reanalyses, and a regional climate model, Atmospheric Chemistry and Physics, 22, 441–463, https://doi.org/10.5194/acp-22-441-2022, 2022.

Wendisch, M., Handorf, D., Tegen, I., Neggers, R., and Spreen, G.: Glimpsing the Ins and Outs of the Arctic Atmospheric Cauldron, Eos, 102, https://doi.org/10.1029/2021eo155959, 2021.

Wendisch, M., Brückner, M., Crewell, S., Ehrlich, A., Notholt, J., Lüpkes, C., Macke, A., Burrows, J. P., Rinke, A., Quaas, J., Maturilli, M., Schemann, V., Shupe, M. D., Akansu, E. F., Barrientos-Velasco, C., Bärfuss, K., Blechschmidt, A.-M., Block, K., Bougoudis, I., Bozem, H., Böckmann, C., Bracher, A., Bresson, H., Bretschneider, L., Buschmann, M., Chechin, D. G., Chylik, J., Dahlke, S., Deneke, H., Dethloff, K., Donth, T., Dorn, W., Dupuy, R., Ebell, K., Egerer, U., Engelmann, R., Eppers, O., Gerdes, R., Gierens, R., Gorodetskaya, I. V., Gottschalk, M., Griesche, H., Gryanik, V. M., Handorf, D., Harm-Altstädter, B., Hartmann, J., Hartmann, M., Heinold, B., Herber, A., Herrmann, H., Heygster, G., Höschel, I., Hofmann, Z., Hölemann, J., Hünerbein, A., Jafariserajehlou, S., Jäkel, E., Jacobi, C., Janout, M., Jansen, F., Jourdan, O., Jurányi, Z., Kalesse-Los, H., Kanzow, T., Käthner, R., Kliesch, L. L., Klingebiel, M., Knudsen, E. M., Kovács, T., Körtke, W., Krampe, D., Kretzschmar, J., Kreyling, D., Kulla, B., Kunkel, D., Lampert, A., Lauer, M., Lelli, L., von Lerber, A., Linke, O., Löhnert, U., Lonardi, M., Losa, S. N., Losch, M., Maahn, M., Mech, M., Mei, L., Mertes, S., Metzner, E., Mewes, D., Michaelis, J., Mioche, G., Moser, M., Nakoudi, K., Neggers, R., Neuber, R., Nomokonova, T., Oelker, J., Papakonstantinou-Presvelou, I., Pätzold, F., Pefanis, V., Pohl, C., van Pinxteren, M., Radovan, A., Rhein, M., Rex, M., Richter, A., Risse, N., Ritter, C., Rostosky, P., Rozanov, V. V., Donoso, E. R., Saavedra Garfias, P., Salzmann, M., Schacht, J., Schäfer, M., Schneider, J., Schnierstein, N., Seifert, P., Seo, S., Siebert, H., Soppa, M. A., Spreen, G., Stachlewska, I. S., Stapf, J., Stratmann, F., Tegen, I., Viceto, C., Voigt, C., Vountas, M., Walbröl, A., Walter, M., Wehner, B., Wex, H., Willmes, S., Zanatta, M., and Zeppenfeld, S.: Atmospheric and Surface Processes, and Feedback Mechanisms Determining Arctic Amplification: A Review of First Results and Prospects of the (AC)3 Project, Bulletin of the American Meteorological Society, 104, E208–E242, https://doi.org/10.1175/bams-d-21-0218.1, 2023.

Wong, S., Genio, A. D. D., Wang, T., Kahn, B. H., Fetzer, E. J., and L'Ecuyer, T. S.: Responses of Tropical Ocean Clouds and Precipitation to the Large-Scale Circulation: Atmospheric-Water-Budget-Related Phase Space and Dynamical Regimes, Journal of Climate, 29, 7127–7143, https://doi.org/10.1175/jcli-d-15-0712.1, 2016.

Woods, C. and Caballero, R.: The Role of Moist Intrusions in Winter Arctic Warming and Sea Ice Decline, Journal of Climate, 29, 4473–4485, https://doi.org/10.1175/jcli-d-15-0773.1, 2016.

You, C., Tjernström, M., and Devasthale, A.: Warm and moist air intrusions into the winter Arctic: a Lagrangian view on the near-surface energy budgets, Atmospheric Chemistry and Physics, 22, 8037–8057, https://doi.org/10.5194/acp-22-8037-2022, 2022.

Zhang, C., Tung, W.-W., and Cleveland, W. S.: Atlas of Arctic Atmospheric River Climatology Based on ERA5 and MERRA-2, https://doi.org/10.1002/essoar.10511981.1, 2022.

Zheng, M., Monache, L. D., Wu, X., Ralph, F. M., Cornuelle, B., Tallapragada, V., Haase, J. S., Wilson, A. M., Mazloff, M., Subramanian, A., and Cannon, F.: Data Gaps within Atmospheric Rivers over the Northeastern Pacific, Bulletin of the American Meteorological Society, 102, E492–E524, https://doi.org/10.1175/bams-d-19-0287.1, 2021.